

COLD GASS, an IRAM Legacy Survey of Molecular Gas in Massive Galaxies: II. The non-universality of the Molecular Gas Depletion Timescale

Amélie Saintonge^{1,2*}, Guinevere Kauffmann¹, Jing Wang^{1,3}, Carsten Kramer⁴, Linda J. Tacconi², Christof Buchbender⁴, Barbara Catinella¹, Javier Graciá-Carpio², Luca Cortese⁵, Silvia Fabello¹, Jian Fu^{6,1}, Reinhard Genzel², Riccardo Giovanelli⁷, Qi Guo^{8,9}, Martha P. Haynes⁷, Timothy M. Heckman¹⁰, Mark R. Krumholz¹¹, Jenna Lemonias¹², Cheng Li^{6,13}, Sean Moran¹⁰, Nemesio Rodriguez-Fernandez¹⁴, David Schiminovich¹², Karl Schuster¹⁴ and Albrecht Sievers⁴

¹Max-Planck Institut für Astrophysik, 85741 Garching, Germany

²Max-Planck Institut für extraterrestrische Physik, 85741 Garching, Germany

³Center for Astrophysics, University of Science and Technology of China, 230026 Hefei, China

⁴Instituto Radioastronomía Milimétrica, Av. Divina Pastora 7, Nucleo Central, 18012 Granada, Spain

⁵European Southern Observatory, Karl-Schwarzschild-Str. 2, 85748 Garching, Germany

⁶Key Laboratory for Research in Galaxies and Cosmology, Shanghai Astronomical Observatory, Chinese Academy of Sciences, Nandan Road 80, Shanghai 200030, China

⁷Center for Radiophysics and Space Research, Cornell University, Ithaca, NY 14853, USA

⁸National Astronomical Observatories, Chinese Academy of Sciences, Beijing 100012, China

⁹Institute for Computational Cosmology, Department of Physics, Durham University, South Road, Durham DH1 3LE, UK

¹⁰Johns Hopkins University, Baltimore, Maryland 21218, USA

¹¹Department of Astronomy and Astrophysics, University of California, Santa Cruz, CA 95064, USA

¹²Department of Astronomy, Columbia University, New York, NY 10027, USA

¹³Max-Planck-Institut Partner Group, Shanghai Astronomical Observatory

¹⁴Institut de Radioastronomie Millimétrique, 300 Rue de la piscine, 38406 St Martin d'Hères, France

13 August 2018

ABSTRACT

We study the relation between molecular gas and star formation in a volume-limited sample of 222 galaxies from the COLD GASS survey, with measurements of the CO(1-0) line from the IRAM 30m telescope. The galaxies are at redshifts $0.025 < z < 0.05$ and have stellar masses in the range $10.0 < \log M_*/M_\odot < 11.5$. The IRAM measurements are complemented by deep Arecibo HI observations and homogeneous SDSS and GALEX photometry. A reference sample that includes both UV and far-IR data is used to calibrate our estimates of star formation rates from the seven optical/UV bands. The mean molecular gas depletion timescale ($t_{dep}(\text{H}_2)$) for all the galaxies in our sample is 1 Gyr, however $t_{dep}(\text{H}_2)$ increases by a factor of 6 from a value of ~ 0.5 Gyr for galaxies with stellar masses of $\sim 10^{10}M_\odot$ to ~ 3 Gyr for galaxies with masses of a few $\times 10^{11}M_\odot$. In contrast, the atomic gas depletion timescale remains constant at a value of around 3 Gyr. This implies that in high mass galaxies, molecular and atomic gas depletion timescales are comparable, but in low mass galaxies, molecular gas is being consumed much more quickly than atomic gas. The strongest dependences of $t_{dep}(\text{H}_2)$ are on the stellar mass of the galaxy (parameterized as $\log t_{dep}(\text{H}_2) = (0.36 \pm 0.07)(\log M_* - 10.70) + (9.03 \pm 0.99)$), and on the specific star formation rate. A single $t_{dep}(\text{H}_2)$ versus sSFR relation is able to fit both “normal” star-forming galaxies in our COLD GASS sample, as well as more extreme starburst galaxies (LIRGs and ULIRGs), which have $t_{dep}(\text{H}_2) < 10^8$ yr. Normal galaxies at $z=1-2$ are displaced with respect to the local galaxy population in the $t_{dep}(\text{H}_2)$ versus sSFR plane and have molecular gas depletion times that are a factor of 3-5 times longer at a given value of sSFR due to their significantly larger gas fractions.

Key words: galaxies: fundamental parameters – galaxies: evolution – galaxies: ISM – radio lines: galaxies – surveys

1 INTRODUCTION

The physics governing the formation of stars is highly non-linear and operates over a vast range in physical scale. The size of the self-gravitating cores of molecular clouds in which individual stars form is only ~ 0.1 pc and the evolution of these cores is governed by an array of highly complex physical processes: turbulence and magnetic fields in the interstellar medium may regulate the rate of collapse of these structures, while winds, jet-like outflows, radiation pressure and ionizing radiation from the most massive stars will act to suppress the formation of young stars (see McKee & Ostriker 2007, for a recent review).

It is therefore not surprising that the rate at which gas is being converted to stars in a single galaxy exhibits large scatter from one region to another when studied on small scales (e.g. Schruha et al. 2010). What is perhaps more remarkable is the fact that once the smoothing scale exceeds a radius of ~ 1 kpc, well-defined relations between star formation and the *global* gaseous properties of galaxies begin to appear.

The first study of large-scale star formation in galaxies was by Schmidt (1959), who studied the relative distribution of atomic gas and young stars perpendicular to the galactic plane, and derived a power-law relation between the rate of star formation and the volume density of interstellar gas with exponent $n \sim 2$. Almost all studies since then have compared the surface density of newly-formed stars with that of the total (atomic+molecular) cold gas (e.g. Kennicutt 1989, 1998b; Kennicutt et al. 2007; Bigiel et al. 2008). These studies have confirmed the existence of a power-law relation of the form $\Sigma_{\text{SFR}} = a \Sigma_{\text{gas}}^N$, with N generally in the range 1.3-1.4.

It should be noted, however, that the exponent in the power law is quite sensitive to the gaseous tracer that is used, as well as to the type of galaxy under investigation and the size scale being considered. The steepest relations are generally obtained for lower mass disk galaxies in which atomic hydrogen dominates the total gas surface density (Kennicutt 1989; Leroy et al. 2008). In the inner disks of the more massive nearby spirals, molecular gas dominates. In recent work that made use of high-resolution HI, CO, $24\mu\text{m}$ and UV maps of nearby spiral galaxies, Bigiel et al. (2008) found that Σ_{SFR} and Σ_{H_2} were related by a power law relation with $N = 1$, i.e. they found that H_2 appeared to form stars at a constant efficiency. The range of Σ_{H_2} over which this relation was applicable was between 3 and $50 M_{\odot} \text{pc}^{-1}$, i.e. significantly lower than gas densities in starburst galaxies. In samples of infrared-selected galaxies, including ultra-luminous infrared galaxies with $L_{\text{IR}} > 10^{12} L_{\odot}$, there is an almost linear relation between star formation rate and the total amount of very dense molecular gas traced by HCN rather than by CO (Gao & Solomon 2004; Graciá-Carpio et al. 2008). Taken together, these results may imply that the amount of dense gas available for star formation is higher in more actively star-forming galaxies, but that SFR in the *very densest phases* may be independent of global galaxy properties (McKee & Ostriker 2007).

Most of these results are, however, based on the study of single or of relatively small samples of objects with similar properties (either nearby star-forming spiral galaxies or IR-selected samples of starbursting systems). Re-

cently, Schiminovich et al. (2010) studied the relation between atomic gas content and star formation using an unbiased volume-limited sample of galaxies with $M_* > 10^{10} M_{\odot}$ from the *GALEX* Arecibo SDSS Survey (GASS). They found an average HI gas consumption timescale of ~ 3 Gyr. Although the galaxy-to-galaxy scatter around this average value was large, they did not find any dependence of the efficiency with which HI is converted into stars on parameters such as stellar mass, stellar mass surface density, colour, and concentration index. This result is perhaps not surprising, since the atomic gas is one step removed from the actual star formation process.

The relation between atomic gas, H_2 and star formation was also extensively investigated by the THINGS/HERACLES team in a series of papers (Walter et al. 2008; Leroy et al. 2008; Bigiel et al. 2008; Leroy et al. 2009). In their sample, the HI-to- H_2 ratio varies with radius, stellar surface density and pressure. These authors suggested that mechanisms occurring at the GMC scale were responsible for these trends (Leroy et al. 2008). Another possible scenario is that some fraction of the atomic gas in galaxies should be regarded as repository of baryonic material that has been accreted from the surrounding intergalactic medium. Theory predicts that this material resides predominantly in the outer regions of galaxies (e.g. Mo et al. 1998) and much of it therefore has not yet reached high enough densities for self-shielding from the ambient UV field to permit molecule formation to take place (e.g. Fu et al. 2010).

Once molecular gas is formed, however, the picture painted by the THINGS/HERACLES analyses of normal spirals is very simple: one would expect star formation to occur at a rate that would deplete the H_2 in a universal timescale of ~ 2 Gyr (Leroy et al. 2008; Bigiel et al. 2008). Intriguingly, the same universal timescale also appears to hold for the “normal” population of star-forming disk galaxies at redshifts $1 < z < 2$ (Genzel et al. 2010).

We are conducting the COLD GASS survey, which will obtain CO(1-0) line measurements and hence the molecular gas content of a sample of ~ 350 massive galaxies ($10.0 < \log M_*/M_{\odot} < 11.5$) using the IRAM 30m telescope. The details of the survey, data for the first half of the sample, and first science results were presented in Saintonge et al. (2011) (hereafter, Paper I). Since the COLD GASS sample is selected only by stellar mass, it enables us to study the relation between molecular gas and star formation for a representative sample of galaxies, and to test whether the universal depletion timescale that is observed to hold when the data is smoothed on scales of a few hundred parsecs in small samples of nearby spirals, is truly applicable to the galaxy population at large.

In Section 2 we describe the COLD GASS sample of local massive galaxies and present the different data sets and measurements used in this paper. In Section 3 we present our main result concerning the non-universality of the molecular gas depletion timescale, which we summarize in Section 5 and discuss in Section 6. Finally, in Section 4 we compare our results for the large and unbiased COLD GASS sample with results from the literature on molecular gas depletion timescales in normal and starburst galaxies, both at low and at high redshifts. Throughout the paper, distance-dependent quantities are calculated for a standard flat Λ CDM cosmol-

ogy with $H_0 = 70 \text{ km s}^{-1} \text{ Mpc}^{-1}$, and we adopt a conversion factor from CO luminosity to H_2 mass of $\alpha_{CO} = 3.2 M_\odot (\text{K km s}^{-1} \text{ pc}^2)^{-1}$ (which does not account for the presence of Helium), unless otherwise specified.

2 DATA

The COLD GASS sample is stellar mass-selected ($M_* > 10^{10} M_\odot$) and volume-limited ($0.025 < z < 0.050$). The galaxies are selected from the area of sky covered by the SDSS, the GALEX Medium Imaging Survey (MIS) and the ALFALFA HI survey. This provides us with optical imaging and spectroscopy (over the central $3''$) for all galaxies in our sample, as well as HI fluxes for the most gas-rich systems. For the remaining galaxies, the HI data is obtained through pointed observations at the Arecibo observatory as part of the GASS survey (Catinella et al. 2010). The sample used here contains the 222 galaxies presented in Paper I. The sample selection, observations and data products are fully described in that paper, but we present a short recapitulation here.

2.1 Optical and UV photometry

Parameters such as redshifts, sizes, magnitudes, and Galactic extinction factors are retrieved from the SDSS DR7 database (Abazajian et al. 2009). The UV data are taken from the GALEX All-sky and Medium Imaging surveys (AIS and MIS, respectively, see Martin et al. 2005). The SDSS and GALEX images are, however, reprocessed following Wang et al. (2010), in order to obtain accurate UV/optical matched-aperture photometry. This process includes accurately registering the GALEX and SDSS images and smoothing them so that they have the same resolution. In practice, the SDSS r -band images are convolved to the resolution of the GALEX UV images before SExtractor is used to calculate magnitudes in consistent apertures, therefore ensuring that measurements in different bands cover the same physical regions of the galaxies. The derived NUV- r colours are corrected for Galactic extinction using the prescription of Wyder et al. (2007) (see also Catinella et al. 2010). Stellar masses are calculated from the SDSS photometry using the technique of Salim et al. (2007) assuming a Chabrier IMF. The optical- and UV-derived quantities used throughout this study are published in Table 1 of Paper I.

In this study, we also consider morphological parameters derived for the GASS sample by Wang et al. (2010), following the technique of Lotz et al. (2004). The asymmetry parameter (Asym) provides a measure of the difference between the SDSS g -band image of a galaxy and a copy of the same image, rotated by 180° . The larger the value of Asym, the more asymmetric the galaxy. The other parameter we investigate in our analysis is smoothness (Smth), computed from the difference between the original g -band image and a copy of the same image smoothed to a scale of 20% of the petrosian radius. Galaxies with clumpier morphologies therefore have larger values of Smth.

2.2 Optical spectroscopy

For 113 of the COLD GASS galaxies in the present sample, long-slit optical spectra were obtained with the MMT 6.5m and the Apache Point Observatory (APO) 3.5 m telescopes. The spectra were taken along the major axis of the galaxies and cover the wavelength range 3900-7000 Å. Data reduction includes standard procedures: biasing, flat-fielding, cosmic ray rejection, background estimation, and finally registration and co-addition of the individual frames. Flux calibration is achieved through observations of spectrophotometric standard stars and by bootstrapping to SDSS photometry measured through equivalent apertures. These final calibrated spectra are then fitted with a family of templates derived from Bruzual & Charlot (2003) stellar population models following the approach of Tremonti et al (2004) and Brinchmann et al. (2004). After subtraction of the stellar continuum, the strength of key emission features is measured by Gaussian fitting and the emission line fluxes are corrected for dust extinction using the measured Balmer decrement. These procedures are described in detail in Moran et al. (2010).

2.3 Arecibo observations

The HI observations are described in detail in Catinella et al. (2010), so we only provide a brief overview here. The GASS survey builds upon existing HI databases: the Cornell digital HI archive (Springob et al. 2005) and the ALFALFA survey (Giovanelli et al. 2005). HI data for about 20% of the GASS sample (the most gas-rich objects), can be found in either of these sources. For the rest of the sample, observations are carried out at the Arecibo Observatory. Integration times are set so as to detect HI gas mass fractions ($f_{\text{HI}} = M_{\text{HI}}/M_*$) of 1.5% or more. Observations are carried out using the L -band Wide receiver and the interim correlator, providing coverage of the full frequency interval of the GASS targets at a velocity resolution of 1.4 km s^{-1} before smoothing. Data reduction includes Hanning smoothing, bandpass subtraction, radio frequency interference (RFI) excision, flux calibration and weighted combination of individual spectra. Total HI-line fluxes, velocity widths and recessional velocities are then measured using linear fitting of the edges of the HI profiles (e.g. Springob et al. 2005; Catinella et al. 2007).

2.4 IRAM 30m observations

We measure the CO(1-0) rotational transition line using the IRAM 30m telescope and its Eight Mixer Receiver (EMIR). As a backend, we use the Wideband Line Multiple Autocorrelator (WILMA), giving a resolution of 2 MHz ($\sim 5 \text{ km s}^{-1}$ at the observing frequency). We also simultaneously record the data with the 4MHz Filterbank, as a backup. With a single tuning of the receiver at a frequency of 111.4081 GHz, we are able to detect the redshifted CO(1-0) line for all the galaxies in our sample ($0.025 < z < 0.05$), within the 4 GHz bandwidth covered by the spectrometers. We integrate on each galaxy until the first of the following three conditions is met: (1) the CO line is detected with $S/N > 5$, (2) sensitivity to a molecular gas mass fraction (M_{H_2}/M_*) of 1.5% is achieved, or (3) an absolute minimum rms of 1.1mK (per

20 km s⁻¹-wide channel) is reached. For most galaxies, the total CO line flux can be recovered by a single pointing of the IRAM 30m telescope. For the most extended objects, a second pointing is performed, offset by 16'' along the major axis. A set of models is used to apply the appropriate aperture corrections based on these measurements.

The data are reduced with the CLASS/GILDAS¹ software. All scans are visually examined, and those with distorted baselines, increased noise due to poor atmospheric conditions, or anomalous features are discarded. The individual scans for a single galaxy are baseline-subtracted (first order fit) and then combined. This averaged spectrum is finally binned to a resolution of ~ 20 km s⁻¹.

The flux in the CO(1-0) line is measured by adding the signal within an appropriately defined windowing function. If the line is detected, the window is set by hand to match the observed line profile. If the CO line is undetected or very weak, the window is set either to the full width of the HI line (W_{50HI}) or to a width of 300 km s⁻¹ in case of an HI non-detection. The detection rate of the CO line is 54%, but our observing strategy allows us to set a stringent upper limit in the case of a non detection.

After correcting the CO(1-0) line fluxes (or upper-limits) for aperture effects, using a set of models derived from a compilation of nearby galaxies with resolved maps, total CO luminosities L'_{CO} are calculated following Solomon et al. (1997). The total molecular hydrogen masses are then calculated as $M_{H_2} = L'_{CO} \alpha_{CO}$. We adopt a constant Galactic conversion factor of $\alpha_{CO} = 3.2 M_{\odot} (\text{K km s}^{-1} \text{pc}^2)^{-1}$, which does not include a correction for the presence of Helium.

An extensive description of the IRAM observing procedure and of the data reduction steps can be found in Paper I. The CO line fluxes and molecular gas masses for all the galaxies in this study are given in Table 2 of Paper I.

2.5 Star formation rates

Star formation rates for all COLD GASS galaxies are calculated from optical/UV spectral energy distribution (SED) fitting (SFR_{SED}). The technique is explained in detail in Appendix A. In short, fluxes in the seven SDSS and GALEX bands are fitted with a series of model SEDs constructed from the Bruzual & Charlot (2003) population synthesis code, assuming a range of star formation histories, ages, metallicities and dust attenuation factors. As described in the Appendix, the assumed distribution of dust attenuation factors is the critical factor in obtaining accurate star formation rates using this method. We use the sample of Johnson et al. (2007) to calibrate our dust attenuation priors. This dataset includes GALEX FUV data, plus 8, 24 and 70 μm data from Spitzer for a representative sample of galaxies selected from SDSS. For galaxies with $\text{NUV}-r < 5$, our values of SFR_{SED} are consistent with the total star formation rates (SFR_{tot}) derived from the combined GALEX FUV and Spitzer 70 μm fluxes, with scatter of only 0.22 dex (see Appendix A and Figure A1).

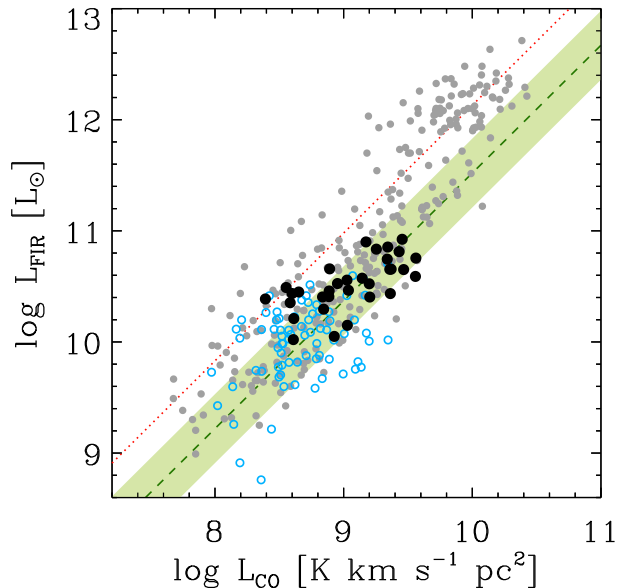


Figure 1. Relation between CO luminosity and far-infrared (FIR) luminosity. Small gray circles show the compilation of normal and luminous infrared galaxies presented in Graciá-Carpio et al. (2011). The dashed line shows the relation derived by Genzel et al. (2010) for normal galaxies (the shaded region denotes the 1σ scatter about this relation); the dotted line is the relation derived by the same authors for ULIRGs/merging systems. COLD GASS galaxies with IRAS measurements are overplotted as filled circles and are seen to follow the same trend. For the remainder of the COLD GASS sample (open blue circles), we “infer” L_{FIR} from the total star formation rate after subtracting the component contributed by the observed UV radiation (without attenuation correction).

2.6 Comparison with infrared luminosity

For a small fraction of the COLD GASS sample ($\sim 15\%$), flux measurements at 60 and 100 μm can be found in the IRAS Faint Source Catalog (Moshir et al. 1992). The far-infrared luminosity inferred from these fluxes is an excellent measurement of the total luminosity from young stars that has been reprocessed by dust, and is known to correlate well with the total CO luminosity of the galaxies (e.g. Sanders & Mirabel 1985; Sanders et al. 1991; Gao & Solomon 2004). In Figure 1, we plot the $L_{FIR} - L_{CO}$ relation for the COLD GASS sample and compare it to literature results for a collection of nearby galaxies. The COLD GASS galaxies with IRAS measurements (filled circles in Figure 1) follow previously derived relations almost exactly. The rms scatter about the relation is 0.30 dex, compared to the value of 0.31 dex derived for reference samples of nearby galaxies (Genzel et al. 2010).

For the COLD GASS galaxies without IRAS measurements, we *infer* L_{FIR} by assuming that it should be equal to $(\text{SFR}_{SED} - \text{SFR}_{UV})$. These estimates are plotted as open symbols in Figure 1. For the sample, the scatter around the Genzel et al. (2010) relation is 0.39 dex. This enhanced scatter could be due to the uncertainty in the values of SFR_{SED} (see Appendix A); only direct infrared measurements of these galaxies will allow us to firmly establish the

¹ <http://www.iram.fr/IRAMFR/GILDAS>

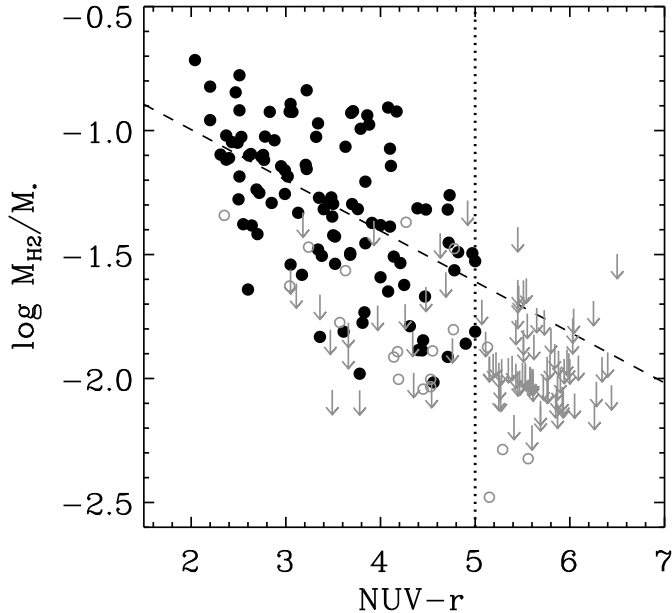


Figure 2. Molecular gas mass fraction as a function of $\text{NUV}-r$ colour for the current COLD GASS sample of 222 galaxies. Secure detections are represented as filled circles, tentative detections as open circles, and non-detections as 5σ upper limits as indicated by the arrows. The best fit linear regression is overplotted, as well as the empirical threshold of $\text{NUV}-r=5$ which marks an abrupt transition from the gas-rich, star forming population to a more passive population.

level of scatter in the $L_{\text{CO}} - L_{\text{FIR}}$ relation for our complete sample. Nevertheless, Figure 1 makes it clear that our sample spans a broader range in properties such as star formation rate compared to IRAS-selected samples. As we will show in Section 3, our samples also include galaxies with a wider range of CO-to-IR luminosities or, equivalently, molecular gas mass to star formation rate ratios.

2.7 Molecular gas depletion timescales

Using the molecular hydrogen gas masses (or upper limits) and the star formation rates derived from SED fitting, we define for each galaxy its molecular gas depletion timescale:

$$t_{\text{dep}}(\text{H}_2) \equiv M_{\text{H}_2} \text{SFR}_{\text{SED}}^{-1}. \quad (1)$$

This parameter therefore describes how long each galaxy could sustain star formation at the current rate before running out of fuel, assuming that the gas reservoir is not replenished. Some studies instead consider the inverse of $t_{\text{dep}}(\text{H}_2)$, the molecular gas star formation efficiency (SFE_{H_2}). However, since the definition of SFE is not universal, with some authors quoting SFE as a dimensionless quantity per dynamical time, we use in this study the more straightforwardly-defined depletion timescale, defined in Equation 1. Similarly, the atomic gas depletion timescale is $t_{\text{dep}}(\text{HI}) \equiv M_{\text{HI}} \text{SFR}_{\text{SED}}^{-1}$.

2.8 Sample definition

One of the key results of Paper I is presented in Figure 2. We found sharp thresholds in galaxy parameters such as stellar mass (M_*), stellar mass surface density (μ_*), concentration index (R_{90}/R_{50}) and colour, below which almost all galaxies have a measurable cold gas component but above which the detection rate of the CO line drops suddenly. These thresholds correspond approximately to the transition between blue cloud and red sequence. The strongest bimodality is seen when relating the molecular gas mass fraction and the $\text{NUV}-r$ colour of the galaxies (Figure 2). A clear threshold at $\text{NUV}-r=5$ marks a break between the star forming and the passive populations.

This colour threshold is also the limit where the uncertainty on the SED fitting-derived star formation rates increases abruptly (Figure A1). Galaxies with $\text{NUV}-r > 5$ only have upper limits for M_{H_2} and very uncertain measures of SFR, therefore their depletion times (Equation 1) are very poorly constrained. From here on, we therefore consider only the subset of COLD GASS galaxies which have $\text{NUV}-r < 5$ and which make up the active population. Through stacking, we have shown in Paper I that the passive population is truly “red and dead”, with a stringent constraint on their average gas mass fraction of $M_{\text{H}_2}/M_* = 0.0016 \pm 0.0005$. These red galaxies are therefore mostly irrelevant for the following discussion and we do not consider them further. Galaxies with $\text{NUV}-r < 5$ but no CO detection are considered as upper limits in the $t_{\text{dep}}(\text{H}_2)$ plots, using 5σ upper limits for M_{H_2} (see Paper I).

3 A NON-UNIVERSAL MOLECULAR GAS DEPLETION TIMESCALE

Resolved studies of the disks of normal galaxies indicate that the molecular gas depletion timescale is constant (Bigiel et al. 2008; Leroy et al. 2008). In this section, we investigate how our integrated measurements of $t_{\text{dep}}(\text{H}_2)$ scale with a number of other global physical parameters, including stellar mass, stellar surface mass density, bulge-to-disk ratio and specific star formation rate.

3.1 Variations with global physical parameters

In Figure 3, the molecular gas depletion timescale is plotted against a range of parameters describing the global physical properties of the galaxies. Although there is scatter, a clear dependence of $t_{\text{dep}}(\text{H}_2)$ on many of the parameters is observed. In all cases, we use two different measures to quantify the strength of the dependence of $t_{\text{dep}}(\text{H}_2)$ on the x-axis parameter: (1) the Pearson correlation coefficient of the parameters, r , and (2) the scatter of the residuals in $\log(t_{\text{dep}}(\text{H}_2))$ of the best fit linear relation (regression of y against x), σ . As a comparison point, the scatter in $\log(t_{\text{dep}}(\text{H}_2))$ for all the CO detections is $\sigma = 0.315$ dex. We fit both to the secure detections only, and also to the entire sample of galaxies with $\text{NUV}-r < 5$ including tentative detections and upper limits. The coefficients as well as the parameters of the best-fit relations for both of these (sub-)samples are given in Table 1. All the fits and mean values are computed by weighting

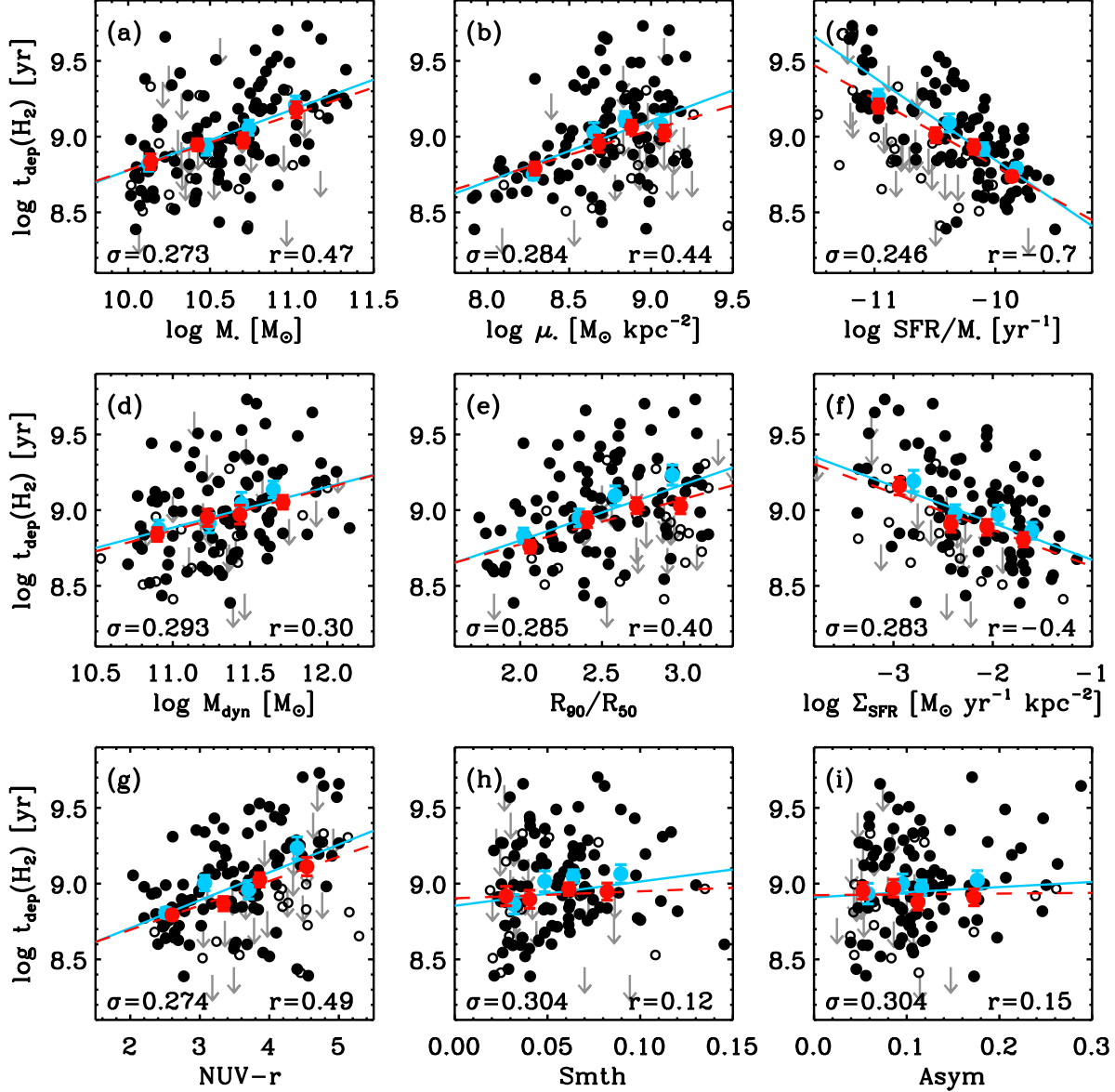


Figure 3. Depletion time for the molecular gas as a function of a variety of parameters. Filled and open black circles indicate COLD GASS secure and tentative detections. We also show the mean values in equally populated bins for secure detections only (blue symbols) and for the entire sample with $\text{NUV-r} < 5$ (red symbols). The error bars indicate 1σ confidence interval on the mean, determined by bootstrapping. The solid and dashed lines are the linear regression of $t_{\text{dep}}(\text{H}_2)$ against the x -axis parameter, for the secure detections only and the entire sample, respectively. In each panel we give the scatter in the residuals of this best-fit relation (σ), as well as the correlation coefficient measured for the secure detections (r).

galaxies differently according to their stellar mass. This procedure, explained in detail in Paper I, corrects for the fact that by selection the COLD GASS sample has a $\log M_*$ distribution which is flatter than in a purely volume-limited sample.

Interestingly, the depletion timescale depends both on parameters that describe the masses and structural properties of the galaxies and on parameters relating to their stellar populations and star formation rates. A clear dependence of $t_{\text{dep}}(\text{H}_2)$ on the stellar mass of the systems is observed ($r = 0.48$), as well as on the presence of a bulge as parametrized by the concentration index, R_{90}/R_{50} ($r = 0.40$), and on pressure within the disk as measured by

the stellar mass surface density, μ_* ($r = 0.44$). In all these cases, the scatter in the residuals of the best-fit relations is significantly smaller than the scatter in $t_{\text{dep}}(\text{H}_2)$ itself. Of these three, the dependence on $\log M_*$ is strongest, and also the most insensitive to the presence of non-detections in CO (see Figure 3a and Table 1).

There is a weaker dependence of $t_{\text{dep}}(\text{H}_2)$ on dynamical mass (Figure 3d, $r = 0.31$), which is estimated as:

$$M_{\text{dyn}} = \frac{v_c^2 R}{G}, \quad (2)$$

where the circular velocities, v_c , are measured from the HI linewidths, $W_{50\text{HI}}$, as:

Table 1. Molecular gas depletion time relations^a

x parameter	units	x_0	All galaxies with $\text{NUV}-r < 5$				Secure detections only			
			m	b	σ	r	m	b	σ	r
$\log M_*$	$\log M_\odot$	10.70	0.36 ± 0.07	9.03 ± 0.99	0.274	0.42	0.40 ± 0.07	9.06 ± 1.03	0.269	0.48
$\log \mu_*$	$\log M_\odot \text{kpc}^{-2}$	8.70	0.33 ± 0.07	8.95 ± 0.91	0.284	0.36	0.40 ± 0.07	8.99 ± 0.88	0.275	0.44
$\log \text{SFR}/M_*$	$\log \text{yr}^{-1}$	-10.40	-0.44 ± 0.04	8.98 ± 0.61	0.246	-0.61	-0.54 ± 0.04	9.06 ± 0.62	0.221	-0.70
$\log M_{dyn}$	$\log M_\odot$	11.40	0.28 ± 0.07	8.98 ± 1.05	0.293	0.31	0.27 ± 0.08	8.99 ± 1.16	0.291	0.31
R_{90}/R_{50}	...	2.50	0.30 ± 0.06	8.92 ± 0.21	0.286	0.34	0.37 ± 0.07	8.99 ± 0.22	0.290	0.40
$\log \Sigma_{\text{SFR}}$	$\log M_\odot \text{yr}^{-1} \text{kpc}^{-2}$	-2.40	-0.24 ± 0.04	8.97 ± 0.15	0.283	-0.43	-0.24 ± 0.06	9.01 ± 0.16	0.287	-0.44
$\text{NUV}-r$	mag	3.50	0.16 ± 0.03	8.94 ± 0.14	0.275	0.42	0.18 ± 0.03	8.98 ± 0.15	0.263	0.49
Smth	...	0.05	0.46 ± 1.01	8.93 ± 0.08	0.304	0.06	1.60 ± 1.28	8.93 ± 0.10	0.307	0.13
Asym	...	0.10	0.05 ± 0.49	8.93 ± 0.08	0.305	0.10	0.34 ± 0.61	8.94 ± 0.09	0.309	0.16

^a The relations are parametrized as $\log t_{dep}(\text{H}_2)[\text{yr}^{-1}] = m(x - x_0) + b$, with all quantities and units given in this table.

$$v_c = \frac{W50_{HI}/2.0}{(1+z)\sin(\text{incl})}. \quad (3)$$

The factor $(1+z)$ accounts for cosmological stretching and the $\sin(\text{incl})$ term is a correction for the inclination of the system (as measured from SDSS photometry). In Equation 2, we further assume that the size of the HI disk (R) is 1.5 times the size of the optical disk ($D_{25}/2$). Uncertainty in this approximation certainly contributes to the scatter of the relation between $t_{dep}(\text{H}_2)$ and M_{dyn} .

The strongest dependencies in Figure 3 are however on quantities that are sensitive to the amount of star formation in the galaxies. The two strongest correlations of $t_{dep}(\text{H}_2)$ are with $\text{NUV}-r$ colour ($r = 0.49$) and with specific star formation rate (sSFR, $r = -0.7$). These quantities are directly linked, because $\text{NUV}-r$ is a good proxy for sSFR since it relates a quantity tracing ongoing star formation activity (NUV flux) and a quantity sensitive to the older stellar population (r -band flux). However, they differ in the sense that the sSFR takes into account internal dust attenuation and the mass-to-light ratio of the old stellar population, while $\text{NUV}-r$ is not corrected for both these effects.

At first glance, $t_{dep}(\text{H}_2)$ seems to depend more strongly on sSFR than on $\text{NUV}-r$ colour, as revealed by the correlation coefficients and scatter around the best fit relations (Table 1). However, we must be cautious because the same measure of the SFR enters in the computation of $t_{dep}(\text{H}_2)$ and sSFR, and the stronger correlation with sSFR compared to $\text{NUV}-r$ may therefore only be induced by this common quantity. We test for this using a Monte-Carlo approach, which aims to decorrelate the errors on $t_{dep}(\text{H}_2)$ and sSFR. To mimic an independent measure of the two parameters, while keeping $t_{dep}(\text{H}_2)$ fixed to the original values, we recompute the sSFR by allowing the star formation rate of each galaxy to vary around the measured value according to the observed measurement error, assuming a normal distribution ($\sigma_{\text{SFR}} = 0.24$ dex, see Figure A1). We perform 5000 iterations and examine the distribution of the correlation coefficients in the simulated relations, which has a median value of $r = -0.61$ as shown in Figure 4. While there is only a 0.5% chance that the original strength of the correlation ($r = -0.71$) is not due to measurement correlation, the probability that the relation is more strongly correlated than the $t_{dep}(\text{H}_2)$ - $\text{NUV}-r$ ($r = 0.49$) or the $t_{dep}(\text{H}_2)$ - M_* ($r = 0.48$) relations is $> 99.9\%$. We therefore conclude that while part of the strength of the correlation between $t_{dep}(\text{H}_2)$ and sSFR is indeed induced by the common measurement of SFR entering both parameters, the relation is still at least if

not more strongly correlated than the next most significant correlations (i.e. those on $\text{NUV}-r$ colour and stellar mass). In Section 3.2 below, we present further evidence for this.

The molecular gas depletion time is also correlated with the star formation surface density, measured within $R_{50}(\text{SFR})$, the radius enclosing half of the total star formation measured for the whole galaxy. This quantity is measured as part of the SFR_{SED} calculation pipeline. The gas surface density, Σ_{gas} , cannot be accurately calculated for the COLD GASS sample since no direct measurement of the size of the gas disks is available. However, since Σ_{gas} and Σ_{SFR} are directly linked through the Kennicutt-Schmidt relation, we can infer from Figure 3f that $t_{dep}(\text{H}_2)$ is a decreasing function of Σ_{gas} .

On the other hand, $t_{dep}(\text{H}_2)$ does not appear to depend on measures of the degree of asymmetry and clumpiness in the galaxies (Figure 3h,i), the scatter of the residuals of these two relations ($\sigma = 0.308$ and 0.306 , respectively) is not significantly reduced compared to the scatter of 0.315 dex in $t_{dep}(\text{H}_2)$ for the whole sample. Such dependencies might have been expected if, for example, spiral density waves or other perturbations in the disk trigger the formation of GMCs and thus contribute locally to a decrease in $t_{dep}(\text{H}_2)$. The fact that we do not see a clear dependence of $t_{dep}(\text{H}_2)$ on our measurements of structure within the disks could mean either that g -band light (the band used to measure Asym and Smth) is not an optimal tracer of these compression events, or else that the effect mostly disappears once averaged over entire galaxies. We note however that this independence of $t_{dep}(\text{H}_2)$ on spiral arm patterns was also reported by Leroy et al. (2008) using resolved data.

To illustrate some of the results presented in Figure 3 graphically, we show in Figure 5 a gallery of SDSS thumbnails of COLD GASS galaxies at their appropriate locations in the $\text{sSFR}-t_{dep}(\text{H}_2)$ plane. The images clearly reveal that galaxies with longer molecular gas depletion times tend to be redder, more massive, and have larger bulges than those with shorter depletion times.

As a final step, we investigate whether third parameter dependences can be found. We analyze whether the residuals of the $\text{sSFR}-t_{dep}(\text{H}_2)$ relation (the tightest correlation found in Figure 3) show any dependence on any of the parameters included in this study (see Figure B1 and details in Appendix B). We do not identify any convincing third parameter dependence.

Our results imply that for a given amount of molecular gas, all galaxies are not equally efficient at processing this

gas into stars. We find an increase in the mean molecular gas depletion timescale by a factor of ~ 6 over the stellar mass range of 10^{10} to $10^{11.5} M_{\odot}$. This implies that galaxies with large stellar masses, red colours, high stellar surface densities and/or older stellar populations will require significantly longer times to turn their molecular gas into stars. The mean depletion timescale in these systems is $t_{dep}(H_2) \sim 3$ Gyr, as compared to the average of ~ 1 Gyr for the sample as a whole, and to the mean value of ~ 0.4 Gyr for galaxies with stellar masses $\sim 10^{10} M_{\odot}$.

3.2 Validation using spectroscopic parameters

In this section, we analyze the behavior of $t_{dep}(H_2)$ as a function of two spectroscopically-derived quantities, which we measure either from SDSS fiber spectroscopy or from the long slit data (see Section 2.2). While SDSS fiber spectra are available for the entire COLD GASS sample, they have the disadvantage of sampling only the central $3''$ of the galaxies. This limitation could bias our results when investigating quantities that vary radially within the disks.

We measure metallicity from strong line ratios using the prescription of Pettini & Pagel (2004):

$$12 + \log(O/H) = 8.73 - 0.32 \log \left(\frac{[OIII]/H_{\beta}}{[NII]/H_{\alpha}} \right). \quad (4)$$

On this scale, a value of $12 + \log(O/H) = 8.66$ corresponds to solar metallicity. In Figure 6a, we plot $t_{dep}(H_2)$ as a function of metallicity measured from both sets of spectra. $t_{dep}(H_2)$ is found to be completely independent of metallicity (the correlation coefficient is $r = 0.01$). In fact, of all parameters investigated (e.g. in Figure 3), metallicity is the one that shows the least degree of correlation with the depletion timescale. This result is reassuring, as a metallicity dependence could have cast some doubt on our assumption of a constant CO-to- H_2 conversion factor (X_{CO}). We remind the reader that the COLD GASS sample only includes galaxies with stellar masses greater than $10^{10} M_{\odot}$ and less than a few $\times 10^{11} M_{\odot}$. The relation between metallicity and stellar mass is rather flat over this regime (Tremonti et al 2004), with the average gas-phase metallicity only increasing by ~ 0.25 dex over 1.5 dex in $\log M_*$.

The spectroscopic data also provide us with information about stellar absorption features, including the strength of the 4000Å break. The strength of this feature varies monotonically with the age of a stellar population of fixed metallicity. If we assume that the galaxies in our sample have had smooth, exponentially declining star formation histories, we can use standard stellar population synthesis models (Bruzual & Charlot 2003) to calibrate a relation between the 4000 Å break strength and sSFR. We have done this both for the fiber and the long-slit measurements of this feature.

This independent estimate of the sSFR can be used as a second validation of the strength of the dependence of $t_{dep}(H_2)$ on the specific star formation rate. In Figure 6b, we show that the relation between $t_{dep}(H_2)$ and sSFR estimated from the 4000 Å break has a correlation coefficient of -0.61, almost as strong as the value of -0.70 measured for the same relation using photometric quantities, and identical to the value estimated using the Monte-Carlo simulations (see Figure 4b). This spectroscopic measurement there-

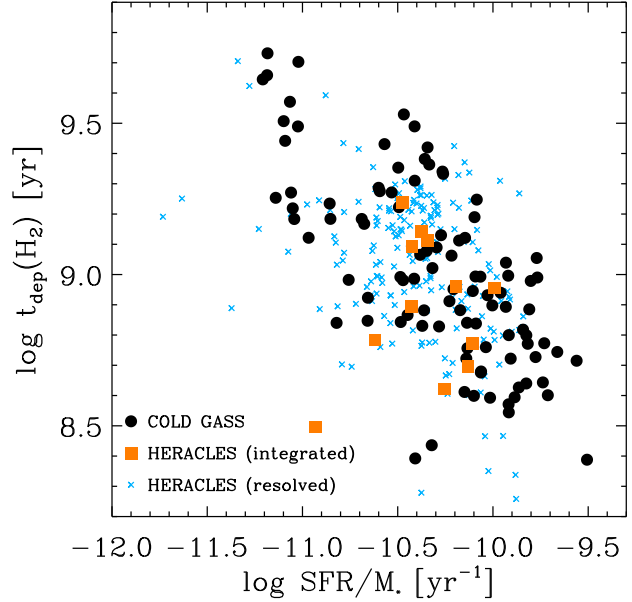


Figure 7. Depletion time for the molecular gas as a function of specific star formation rate for COLD GASS secure detections (filled circles) as well as for the HERACLES sample from Leroy et al. (2008). We plot both the integrated data (filled squares) and the resolved data (crosses). The COLD GASS sample spans a larger range in global values of sSFR than the HERACLES sample. When considering integrated measurements, both data sets however show similar scatter and behaviour in the range of sSFR where they overlap.

fore provides independent confirmation of the effects already seen with $NUV-r$ colour (Figure 3g) and photometrically-derived sSFR (Figure 3c).

3.3 Comparison with resolved studies

We compare our results with those obtained from resolved studies of nearby galaxies. The two approaches are highly complementary: COLD GASS gives us a global picture of gas and star formation in the local Universe, but lacks the power to trace the exact distribution of these components, something surveys like THINGS/HERACLES are designed to do. The methods are however fundamentally distinct, since a volume-limited survey like COLD GASS gives more statistical weight to the lower mass galaxies which naturally dominate the galaxy number density, while a resolved study tends to give more weight to bigger, more massive galaxies which cover more resolution elements. These distinctions should be kept in mind when comparing observations.

While our results show a variation in $t_{dep}(H_2)$, in contrast with the constant H_2 depletion time found for HERACLES survey galaxies (Leroy et al. 2008; Bigiel et al. 2008), the results are not surprising. HERACLES covers a limited range of surface densities typical of nearby “normal” spirals. Observations that probe a wider range of galaxy types have long been known to give different H_2 depletion times between the regimes of normal and “bursty” star formation (e.g. in mergers and ULIRGS, Gao & Solomon 2004), and theoretical models have been able to explain this di-

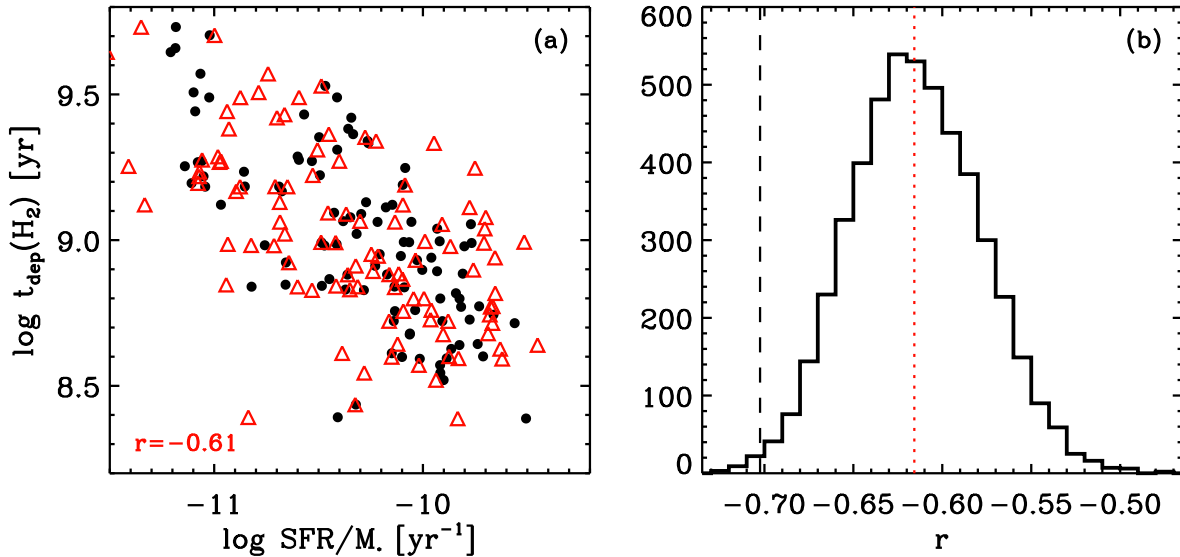


Figure 4. Validation of the $t_{dep}(\text{H}_2)$ -sSFR relation using a Monte-Carlo approach. The correlation coefficient (r) of the original relation is compared to the value measured for a similar relation after decorrelation of the measurement errors. **(a)** An example showing one of the repetitions and comparing the original relation (filled circles) with the “decorrelated” relation (open triangles). **(b)** Distribution of the correlation coefficient of the 5000 iterations (median $r = -0.615$). While there is only a 0.5% chance that the original strength of the correlation ($r = -0.71$) is not due to measurement correlation, the probability that the relation is more strongly correlated than the $t_{dep}(\text{H}_2)$ -NUV- r or the $t_{dep}(\text{H}_2)$ - M_* relations is 99.9%.

chotomy as arising from a transition between galaxies where molecular clouds are gravity-confined to ones where they are pressure-confined (Krumholz et al. 2009). In order to illustrate the consistency of our results with HERACLES, in Figure 7 we directly compare the two data sets. To do this comparison, we plot the depletion timescale as a function of specific star formation rate (sSFR), since this quantity can be reliably compared between the two samples. The comparison shows that the COLD GASS data are perfectly consistent with the HERACLES measurements, once all quantities are brought to a common scale (same conversion factor $\alpha_{CO} = 3.2M_{\odot} (\text{K km s}^{-1} \text{pc}^2)^{-1}$). The reasons why COLD GASS reveals a variable molecular gas depletion timescale are (1) a significantly larger sample, and (2) much larger dynamic range in quantities such as sSFR. We note that Leroy et al. (2008) quote a mean molecular gas depletion time of 1.9 ± 0.9 Gyr. However, after using the same conversion factor and restricting their sample to the COLD GASS stellar mass range, the mean molecular gas depletion time for the HERACLES sample is 0.9 Gyr, perfectly consistent with the COLD GASS estimate (1.05 ± 0.74 Gyr), as seen in Figure 7.

We can gain some further insight by looking at the resolved data from HERACLES, also plotted in Figure 7. Not surprisingly, there is larger scatter in the $t_{dep}(\text{H}_2)$ -sSFR relation, since these points are averages over only \sim kpc-sized regions and not entire galaxies. The resolved data do cover the full range of $t_{dep}(\text{H}_2)$ and sSFR values probed by the COLD GASS galaxies, but the vast majority of the data points are, however, concentrated in the range ($-11.0 < \log \text{SFR}/M_* < -10.0$) and ($8.7 < \log t_{dep}(\text{H}_2) < 9.3$). There are very few regions within these normal star forming spirals that reach values of $t_{dep}(\text{H}_2)$ as low or as high as those seen in the *integrated* COLD GASS measurements. This suggests that large

variations of $t_{dep}(\text{H}_2)$ between different kpc-sized regions of the same galaxies are not common (see also Leroy et al. 2008), and therefore that extreme values on small scales are almost exclusively found in galaxies that are also globally extreme. The few resolved points with depletion times that are unusually high (low) are located in the disk centers (outskirts), where the $M_{\text{H}_2}/M_{\text{H}_1}$ ratio is high (low).

3.4 Comparison with atomic gas depletion time

Another important step in understanding cold gas depletion times in galaxies is the atomic-to-molecular transition. In this section, we compare the molecular and atomic gas depletion timescales across the COLD GASS sample. Schiminovich et al. (2010) studied the behavior of $t_{dep}(\text{HI})$ for galaxies in the GASS survey. They found that the average atomic gas depletion timescale for galaxies with $M_* > 10^{10}M_{\odot}$ is 3 Gyr. There is considerable scatter from one galaxy to another, but the average timescale is a constant function of all quantities investigated.

In Figure 8 we compare the dependencies of $t_{dep}(\text{H}_2)$ and $t_{dep}(\text{HI})$ on M_* , μ_* and NUV- r colour. Not surprisingly, we reproduce well the Schiminovich et al. (2010) result; $t_{dep}(\text{HI})$ does not depend on any of these three quantities and is on average 3 Gyr, although the values of $t_{dep}(\text{HI})$ for individual galaxies range from a few hundred million years to more than a Hubble time. In comparison, the range of values for $t_{dep}(\text{H}_2)$ is smaller, from a few hundred million years to ~ 5 Gyr. This is not surprising, given that the atomic gas-to-stellar mass ratio has much larger dynamic range than the molecular gas-to-stellar mass ratio (Catinella et al. 2010, Paper I).

Using the exact same sample, we can see clearly in Figure 8 that whereas $t_{dep}(\text{HI})$ is constant at ~ 3 Gyr, $t_{dep}(\text{H}_2)$

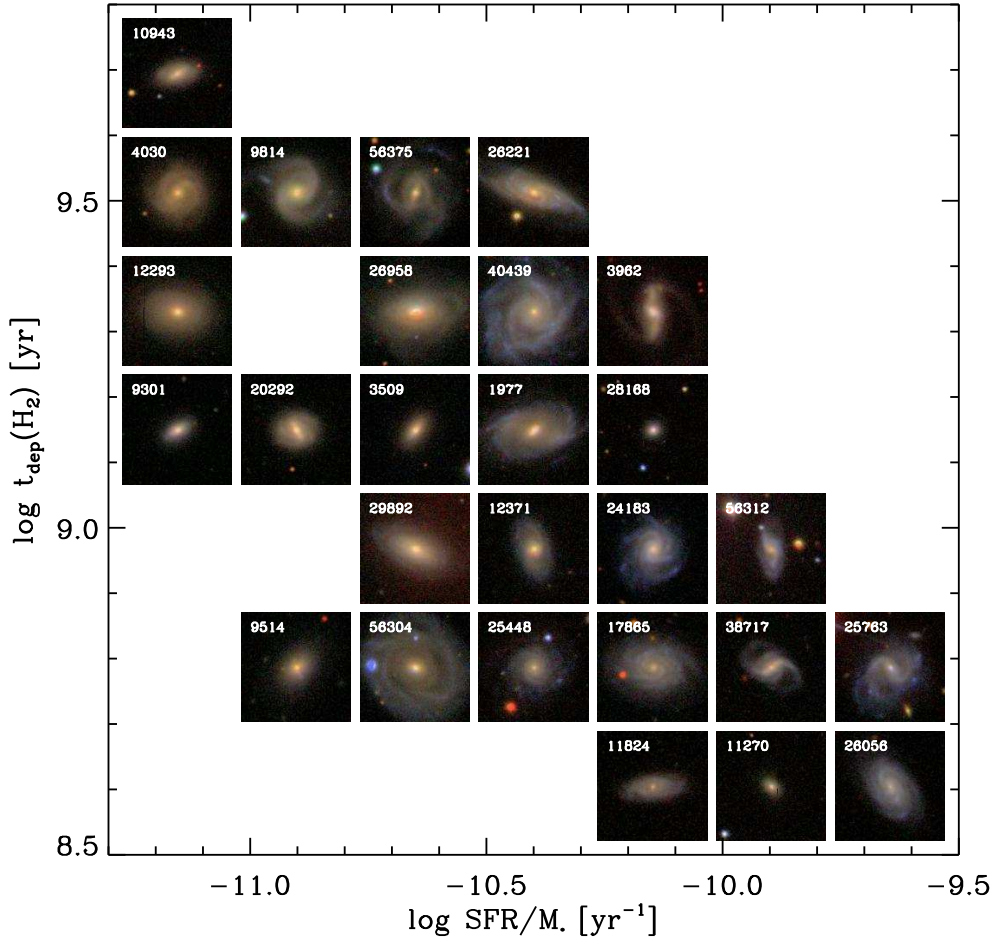


Figure 5. SDSS three-colour images (of dimension 50×50 kpc) of a subset of the COLD GASS galaxies in the $\text{sSFR}-t_{\text{dep}}(\text{H}_2)$ plane. Some of the trends present in Figure 3 are visible: galaxies with the longest depletion times tend to be redder, with early-type morphologies and more prominent bulges.

is a function of all three quantities (M_* , μ_* and $\text{NUV}-r$). It is interesting that at the highest masses, largest surface densities and reddest colours, $t_{\text{dep}}(\text{H}_2) \simeq t_{\text{dep}}(\text{HI})$ for the majority of galaxies. However, for low mass, low stellar surface density and high sSFR galaxies, $t_{\text{dep}}(\text{H}_2)$ is smaller than $t_{\text{dep}}(\text{HI})$ by almost an order of magnitude. In other words, low mass galaxies are much more imminently in danger of running out of molecular gas than out of atomic gas, whereas in high mass systems there appears to be a balance between the consumption rate of atomic and molecular gas (at least when averaged over entire galaxies).

4 BRIDGING LOW AND HIGH REDSHIFT MOLECULAR GAS STUDIES

While direct HI measurements in individual objects are still only possible for nearby galaxies (up to $z \sim 0.3$, Verheijen et al. 2007; Catinella et al. 2008), the detection of CO line emission in galaxies at $z > 1$ is now achievable and will soon become common practice with for example the Atacama Large Millimeter Array (ALMA). Because of the unbiased and homogeneous nature of the sample, COLD GASS will provide an ideal local comparison point for these high redshift studies. In this section, we take a first look at

how the molecular gas depletion times for the galaxies in our sample compare with published results at higher redshifts.

The IRAM Plateau de Bure interferometer is up to now the instrument of choice to perform high redshift CO observations. It has been used to characterize the molecular gas content of submillimeter galaxies (SMGs, e.g. Frayer et al. 1998; Downes & Solomon 2003; Genzel et al. 2003; Neri et al. 2003; Kneib et al. 2005; Tacconi et al. 2008; Bothwell et al. 2010; Engel et al. 2010) and normal star forming galaxies at $z > 1$ (e.g. Tacconi et al. 2010; Genzel et al. 2010; Daddi et al. 2010). In Figure 9 we compare the position of such systems in the $t_{\text{dep}}(\text{H}_2)$ -sSFR plane. To perform this comparison, all data sets need to be put on a common scale. A standard conversion factor of $\alpha_{\text{CO}} = 3.2 M_{\odot} (\text{K km s}^{-1} \text{pc}^2)^{-1}$ is adopted for galaxies with $L_{\text{FIR}} < 10^{12} L_{\odot}$, and a factor of $\alpha_{\text{CO}} = 1.0 M_{\odot} (\text{K km s}^{-1} \text{pc}^2)^{-1}$ is used for the ULIRGs and merging systems (these choices are motivated in e.g. Tacconi et al. 2010; Genzel et al. 2010). The star formation rates are derived from the infrared luminosity for the LIRGs and ULIRGs, and from the 1.4 GHz flux (Chapman et al. 2005) for the SMGs, using the calibration of the FIR-radio correlation of Magnelli et al. (2010).

For both the high and low redshift populations, merging systems (local ULIRGs and high- z SMGs), have much

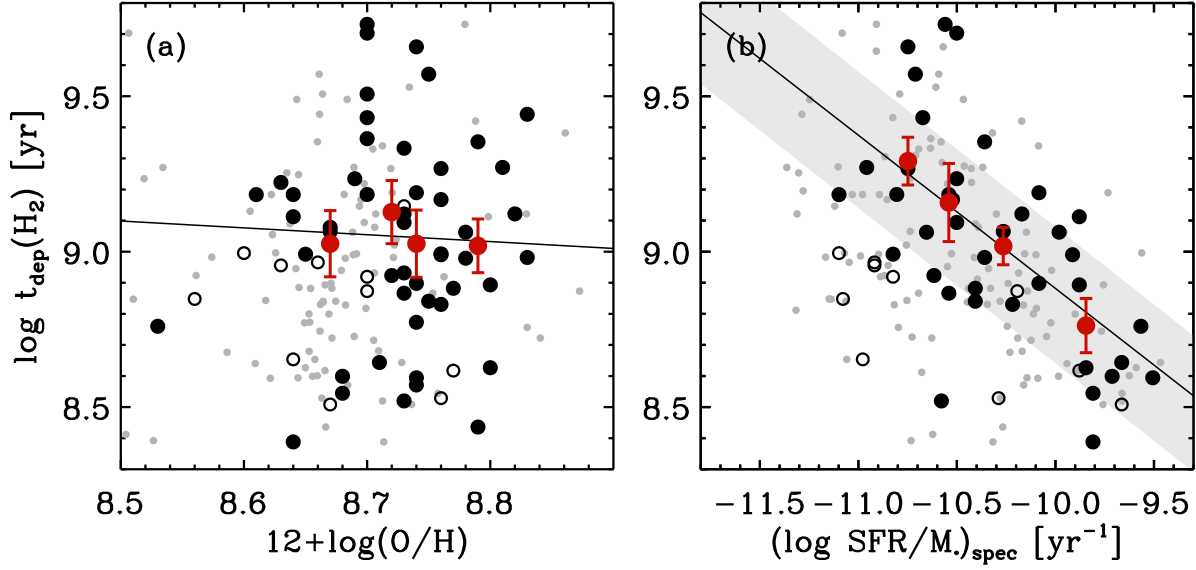


Figure 6. Molecular gas depletion time as a function of two spectroscopic quantities: (a) the gas metallicity calculated using Equation 4 and (b) the sSFR inferred from the measurement of the 4000Å break (see text). The spectroscopic quantities are derived from the SDSS fiber spectroscopy (small gray symbols) and independently from the long-slit spectra (large black symbols, open for tentative CO detections). The solid lines are the best-fitting relations to the latter. In panel (b), as a comparison, the 1σ scatter around the relation of Figure 3c derived using $sSFR_{SED}$ is shown as the shaded region. The spectroscopic data provide an independent confirmation of the trend observed between sSFR and $t_{dep}(H_2)$.

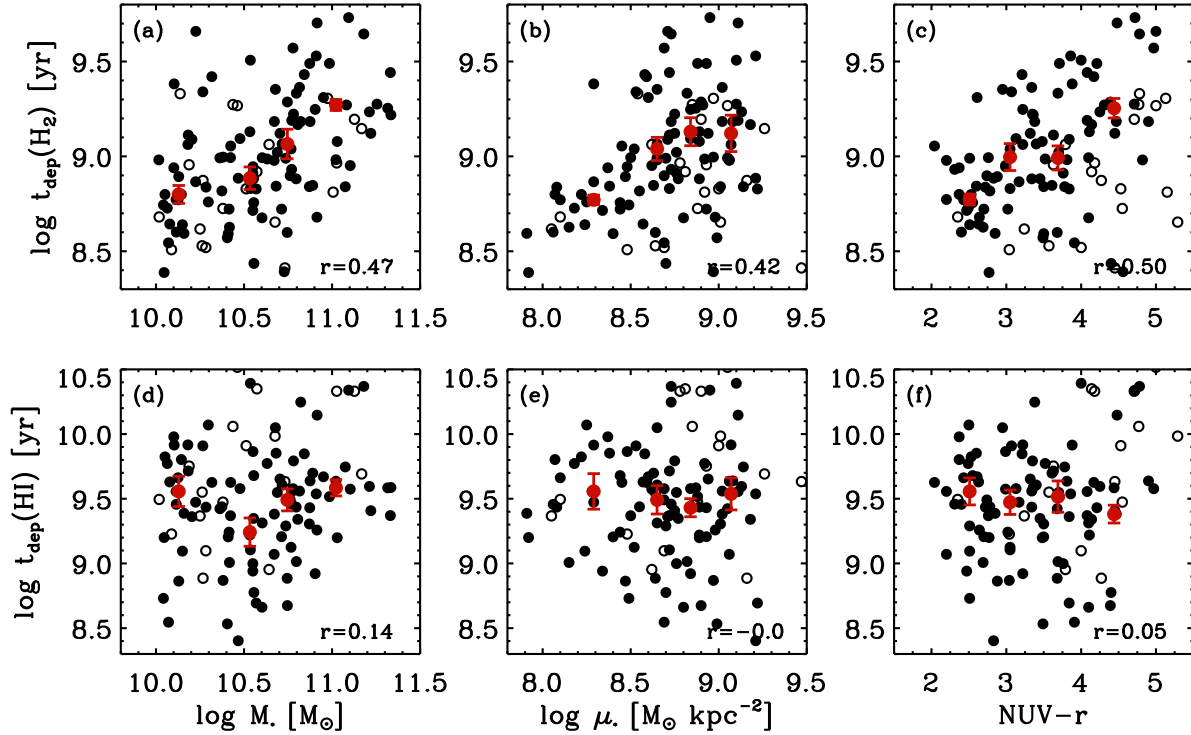


Figure 8. Depletion time for the molecular gas (top row) and atomic gas (bottom row), as a function of (a,d) stellar mass, (b,e) stellar mass surface density and (c,f) NUV- r colour.

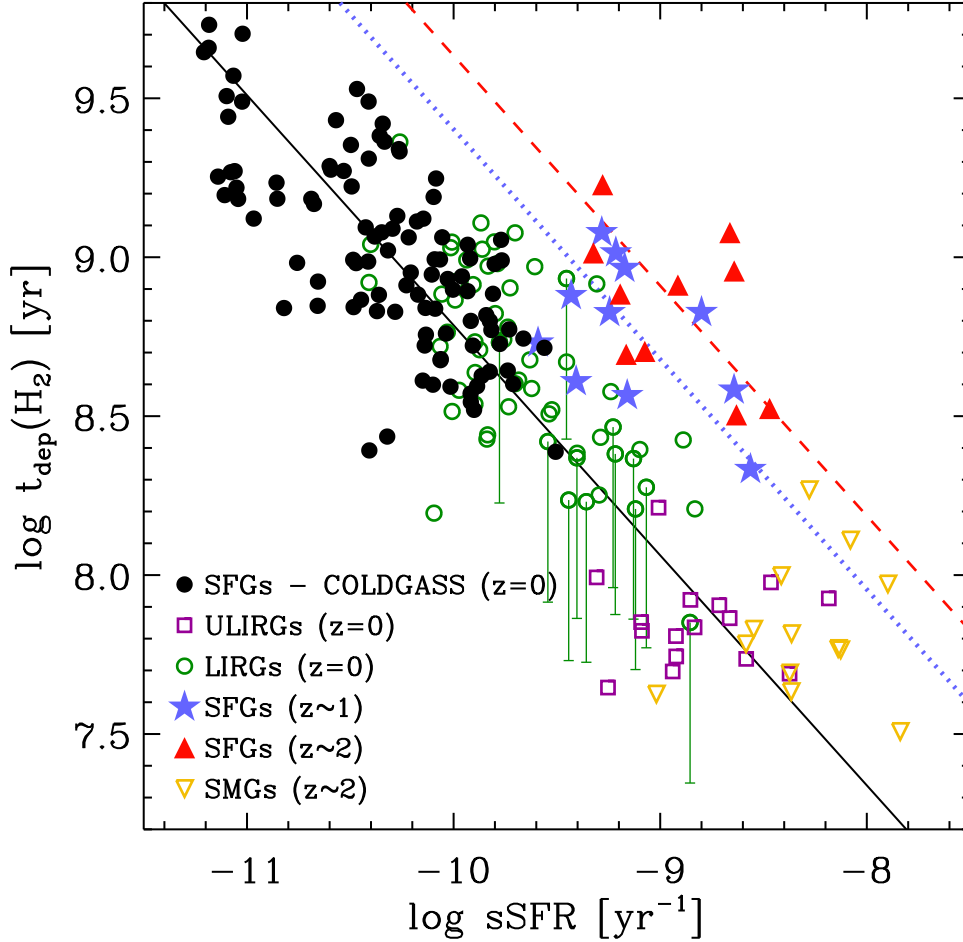


Figure 9. Comparison of the depletion time-specific star formation rate relation, at $z = 0, 1$ and 2 , for normal star forming galaxies and extreme systems (local LIRGs/ULIRGs and high- z SMGs). The best-fit bisector linear relation to the COLD GASS sample, $\log t_{\text{dep}}(\text{H}_2) = (-0.724 \pm 0.039)\text{sSFR} + (1.54 \pm 0.41)$, is plotted as a solid black line. This local relation is evolved to $z = 1$ and 2 (dotted blue and dashed red lines, respectively) using the observed evolution in sSFR with cosmic time (using the relation of Pérez-González et al. 2008). The known offset between the depletion times of normal star-forming galaxies and merging systems (local ULIRGs and high z submillimeter galaxies) is seen, but the population of local LIRGs is found to bridge this gap. A standard conversion factor of $\alpha_{\text{CO}} = 3.2M_{\odot} (\text{K km s}^{-1} \text{pc}^2)^{-1}$ is adopted for galaxies with $L_{\text{FIR}} < 10^{12}L_{\odot}$, and a factor of $\alpha_{\text{CO}} = 1.0M_{\odot} (\text{K km s}^{-1} \text{pc}^2)^{-1}$ is used for the ULIRGs and merging systems (these choices are motivated in e.g. Tacconi et al. 2010; Genzel et al. 2010). The impact of using the smaller conversion factor also for the brightest LIRGs ($L_{\text{FIR}} > 10^{11.75}L_{\odot}$) is shown by a one-sided error bar for each individual object. The high redshift data points are from Genzel et al. (2010) and Hainline et al. (2010), and the local LIRGs/ULIRGs are from Howell et al. (2010) and da Cunha et al. (2010).

shorter depletion timescales than “normal” star-forming galaxies. These two populations of normal and extreme starformers are observed as two distinct branches in the Kennicutt-Schmidt relation (Genzel et al. 2010). Using the measurements of stellar masses of Howell et al. (2010) and da Cunha et al. (2010) for a large sample of local LIRGs, we see that the gap in the relation that extends from the COLD GASS galaxies to the ULIRGs is filled by these galaxies of intermediate infrared luminosities.

We first focus our attention on the “normal” star forming population (filled symbols in Figure 9). The $z = 1 - 2$ galaxies lie at systematically larger values of sSFR as compared to our local comparison samples – this simply reflects the well-studied cosmic evolution of the star forma-

tion versus stellar mass relation (e.g. Noeske et al. 2007; Pérez-González et al. 2008; Rodighiero et al. 2010). In Figure 9, the $t_{\text{dep}}(\text{H}_2)$ -sSFR relation derived for the COLD GASS sample is plotted as a solid line. The dotted and dashed lines show this relation displaced along the x-axis by factors derived based on Pérez-González et al. (2008) for the evolution of the sSFR in blue sequence galaxies out to redshifts of 1 and 2, respectively. Remarkably, the $t_{\text{dep}}(\text{H}_2)$ -sSFR data points for the $z = 1$ and $z = 2$ galaxies lie almost exactly on these “shifted” relations. The reason why normal high redshift galaxies can have relatively long (~ 1 Gyr) molecular gas consumption timescales even though their sSFRs have increased by nearly an order of magnitude, *is because they are so much more gas-rich than nearby objects*

(Tacconi et al. 2010). The only galaxies in our local samples that reach sSFR comparable to the normal high- z star-forming populations are the ULIRGs and some of the more extreme LIRGs, which are almost all dynamically disturbed or interacting systems, with much shorter molecular gas depletion times.

Turning now to the full population of galaxies illustrated in Figure 9, we see that when the COLD GASS sample is combined with samples of low redshift LIRGs and ULIRGs, the $t_{dep}(\text{H}_2)$ versus sSFR relation appears to extend (with much the same slope and even scatter) over another full 1.5 dex in \log sSFR. Instead of a factor 6 range in molecular gas depletion time, there is a factor ~ 50 decrease from the quiescent end of the galaxy population where the present-day star formation rate is only a tenth of its past averaged one, to the most extreme starbursts where the timescale for making the entire stellar mass of the galaxy is 1 Gyr or less. There is a hint that the equivalent extreme galaxies at high- z , the SMGs, may track a different $t_{dep}(\text{H}_2)$ versus sSFR relation – one that is significantly displaced with respect to the relation traced by the normal star-forming galaxies. Or alternatively, the slope of the $t_{dep}(\text{H}_2)$ -sSFR relation may be evolving with redshift. However, testing whether this is the case will require further observations of high redshift galaxies, spanning a wider range of properties, especially extending to lower (specific) star formation rates.

5 SUMMARY OF OBSERVATIONAL RESULTS

A summary of the main empirical results presented in this paper is as follows:

(i) The mean molecular gas depletion timescale for COLD GASS galaxies with $M_* > 10^{10} M_\odot$ and detected CO(1-0) line is 1.05 ± 0.74 Gyr.

(ii) We observe an increase in $t_{dep}(\text{H}_2)$ by a factor of 6 over the stellar mass range of 10^{10} to $10^{11.5} M_\odot$, from ~ 0.5 to ~ 3 Gyr.

(iii) Over the same stellar mass range, the atomic gas depletion timescale remains constant at a value of around 3 Gyr. This means that in high mass galaxies, the molecular and atomic gas depletion timescales are comparable. In low mass galaxies, the molecular gas is being consumed much more quickly than the atomic gas.

(iv) The strongest dependence of $t_{dep}(\text{H}_2)$ is on the specific star formation rate of the galaxy, estimated using either the UV/optical light (corrected for extinction) or the 4000 Å break strength. This relation can be parametrized as $t_{dep}(\text{H}_2) = -0.44(\log \text{SFR}/M_* + 10.40) + 8.98$, where $t_{dep}(\text{H}_2)$ is in units of $\log \text{yr}^{-1}$. There is also a strong dependence on stellar mass: $t_{dep}(\text{H}_2) = (0.36 \pm 0.07)(\log M_* - 10.70) + (9.03 \pm 0.99)$.

(v) We found no significant correlation of the residuals from these relations with any of the global galaxy properties we looked at.

(vi) The $t_{dep}(\text{H}_2)$ versus sSFR relation extends smoothly with the same slope from the sequence of “normal” star-forming galaxies in our COLD GASS sample through to the population of more extreme starburst galaxies (LIRGs and ULIRGs), which have $t_{dep}(\text{H}_2) < 10^8$ yr.

(vii) Normal galaxies at $z=1-2$ are displaced with respect to the local galaxy population in the $t_{dep}(\text{H}_2)$ versus sSFR

plane, in the sense that they have much longer molecular gas depletion times at a given value of sSFR. This is consistent with the fact that these galaxies are much more gas-rich.

6 DISCUSSION

In working towards the understanding of the star formation process, it probably makes sense to break the problem down into two parts: the conversion of atomic gas into molecular form, and the subsequent formation of stars from this cold dense phase. One way to address these issues is through resolved studies of nearby galaxy disks, on sub-kpc scales (e.g. Leroy et al. 2008) or even down to the scale of giant molecular clouds (e.g. Gratier et al. 2010; Schinnerer et al. 2010). Our approach is highly complementary. Only integrated measurements are available to us (total HI, H_2 and stellar masses, for example), but our COLD GASS sample is large, complete, unbiased, and covers a larger region of parameter space than previous studies.

The central result of this paper is that the mean molecular gas depletion timescale ($t_{dep}(\text{H}_2)$) increases by a factor of ~ 6 across the mass range sampled by COLD GASS galaxies, and that this variation correlates strongly with specific star formation rate, $\text{NUV}-r$ colour and stellar mass. Previous surveys were unable to observe this variation or correlation due to the limited dynamic range of their samples. It should be noted however that the non-universality of $t_{dep}(\text{H}_2)$ is perhaps not very surprising. It is well known that gas depletion times are different in extreme starburst galaxies and merging systems in the local Universe, as well as submillimeter galaxies at high redshifts (e.g. Kennicutt 1998b; Riechers et al. 2007; Bouché et al. 2007; Bothwell et al. 2010). In these galaxies, gas depletion times are significantly shorter, with the star formation surface density an order of magnitude larger at fixed gas surface density, compared to the normal galaxy population (Genzel et al. 2010). The novelty of our results lies in showing that $t_{dep}(\text{H}_2)$ varies even within the population of nearby “normal” star forming galaxies, and in quantifying this variation as a function of a range of fundamental parameters.

Our work leaves open the intriguing question of what drives the variability in $t_{dep}(\text{H}_2)$ across our sample. In the smaller range of galaxies explored in the THINGS sample, Bigiel et al. (2008) and Leroy et al. (2008) find a constant molecular gas depletion time. They do not observe any variation in this quantity with respect to galactocentric radius, Toomre Q , or any other galaxy property. This is consistent with the observation by Bolatto et al. (2008) that molecular cloud properties appear essentially invariant across nearby galaxies with properties similar to those in the THINGS sample. In starburst galaxies, however, it is clear that $t_{dep}(\text{H}_2)$ can be much smaller even than the smallest values found in our sample (e.g. Gao & Solomon 2004), and in such systems molecular cloud properties are measurably different than in normal galaxies (e.g. in M64, Rosolowsky & Blitz 2005). We therefore conjecture that the galaxies in our sample that show significantly reduced $t_{dep}(\text{H}_2)$ are those undergoing minor starbursts, and that the weak correlation between $t_{dep}(\text{H}_2)$ and total stellar mass that we observe arises because smaller galaxies have more bursty star formation histories. In what follows, we investi-

gate this possible interpretation of the $t_{dep}(H_2)$ relations, as well as two alternative explanations: quenching in high mass galaxies preventing the molecular gas from efficiently forming stars, and an increasing fraction of molecular gas not traced by the CO(1-0) observations at lower stellar masses.

The first interpretation calls for enhanced star formation efficiency in low mass galaxies due to minor starburst events. This picture is consistent with our result that $t_{dep}(H_2)$ correlates inversely with specific star formation rate, and that the scatter in the relation is largest at low stellar masses. The starbursts in these galaxies would not be the large ones associated with major mergers, but would instead be weaker ones associated with distant tidal encounters, variations in the intergalactic medium accretion rate, or secular processes within galactic disks. Any process capable of driving gas toward the galactic center and raising the surface density there will suffice, since lower depletion times and altered molecular cloud properties are associated with galactic surface densities above $\sim 100 M_\odot \text{ pc}^{-2}$ on both observational and theoretical grounds (Krumholz et al. 2006, 2009).

The second interpretation for the variable $t_{dep}(H_2)$ invokes the higher mass galaxies, and how star formation could be preferentially suppressed in these systems. Morphological quenching (e.g. Martig et al. 2009) and feedback scenarios which prevent the molecular gas from forming stars while at the same time not destroying the gas, would predict that a consequence of the quenching would be an increased reservoir of molecular gas. The specific star formation rate would then inversely correlate with $t_{dep}(H_2)$ as we observe, and we would expect to see some trend with galaxy morphology (e.g. concentration index, R_{90}/R_{50}) which is also seen in Figure 3e.

As a third possible explanation, we ask whether the observed $t_{dep}(H_2)$ trends may be explained by the fact that the CO(1-0) emission line may not be an accurate tracer of the molecular gas content of the low mass galaxies in our sample, which may have systematically lower metallicities than the higher mass galaxies (Tremonti et al. 2004). Krumholz et al. (2011) suggest that CO-inferred molecular gas measurements may begin to miss an increasing fraction of the total H_2 at metallicities as high as half solar (see also Bolatto et al. 2008; Leroy et al. 2011). As discussed in Paper I, the COLD GASS sample is limited to galaxies with stellar masses greater than $10^{10} M_\odot$, so the *global* metallicities of our galaxies are all solar or greater, so this concern is not likely to apply. One might nevertheless still worry that metallicities in the outer regions of the galaxies are lower, so one might still not account for some fraction of the total molecular content of the galaxy. If metallicity gradients were to correlate with for example stellar mass or stellar mass surface density, this might create the dependence of $t_{dep}(CO)$ on those quantities. However, our recent analysis of metallicity gradients using long-slit spectra obtained from MMT (Moran et al., in preparation) indicates that metallicity gradients of the galaxies in our sample are mostly flat and do not correlate strongly with either quantity.

The observed dependence of $t_{dep}(H_2)$ on several parameters such as stellar mass and specific star formation rate, is then likely caused by a combination of the first two effects, each acting at a different end of the COLD GASS stellar mass range. In high mass galaxies, star formation would

preferentially be quenched by internal processes, while in low mass galaxies, star formation would preferentially be enhanced through mild starburst events.

The final mystery in this picture is why $t_{dep}(HI)$ should vary less than $t_{dep}(H_2)$. We note that the invariance of $t_{dep}(HI)$ must break down in sufficiently strong starbursts – for example Arp 220 has a star formation rate of $\sim 50 M_\odot \text{ yr}^{-1}$ (Downes & Solomon 1998), but an HI mass below $4 \times 10^9 M_\odot$ (Baan et al. 1987), giving $t_{dep}(HI) < 100 \text{ Myr}$. However, galaxies like Arp 220 are rare, and we almost certainly do not have any galaxies quite that extreme in our sample. For the weaker starbursts we do include, it seems plausible that the majority of the HI resides in a quiescent outer disk that is largely unaffected by whatever process produces the starburst. It indeed appears that the conversion of atomic to molecular gas is, in some situations, a bottleneck in the star formation process. For example, at low stellar mass surface densities ($\log \mu_* < 8.7$, see Figure 3b), all galaxies have $t_{dep}(H_2)$ shorter than the sample mean of 1 Gyr. These galaxies are processing their molecular gas into stars faster than they are consuming their atomic gas, due to some internal (e.g. bar instabilities) or external (e.g. tidal interactions) processes triggering minor starburst events, as we speculated above. In these galaxies, HI is likely to be accumulating in regions where the conversion between atomic and molecular gas is less efficient and where this gas cannot participate in the the star formation process, for example in the outer disks of galaxies.

Why should HI accumulate more effectively in low mass galaxies than in high mass galaxies? One possibility is that gas from the external environment is able to accrete more efficiently in such systems. At a halo mass of greater than few $\times 10^{11} M_\odot$, gas is expected to shock-heat to the virial temperature of the halo and cooling times become longer (e.g. Kereš et al. 2005). Once the gas has been accreted, the production of molecular gas may rely of gas flows that bring gas from the outer disks to the central regions of the galaxy, where it is able to reach high enough densities to be shielded from the ambient UV radiation field and form molecules. If such gas flows are dynamically driven (e.g. Chakrabarti & Blitz 2009), one might expect them to occur more frequently in high mass galaxies, which are located in more massive halos and more crowded environments. In addition, feedback processes from AGN may disrupt gas accretion in the most massive dark matter halos.

It is also interesting to speculate on the issue of gas accumulation in high redshift galaxies. We have seen that the molecular gas depletion times in normal galaxies at $z = 1-2$ are nearly an order of magnitude longer than in local galaxies with the same specific star formation rates. In nearby starburst galaxies, the very high values of sSFR are achieved because dynamical disturbances act to compress the available interstellar medium into a very small volume, in which the filling factor of GMCs and young stars is presumably very high. Although we have not yet been able to demonstrate this conclusively, our current best guess is that the relation we uncovered between $t_{dep}(H_2)$ and sSFR is simply a reflection of increased dynamical stirring of one sort or another, as one proceeds to more strongly star-forming galaxies. At the extreme high sSFR end of the sequence, clear evidence for recent merging is always seen, but at the low sSFR end, the diagnostics of the dynamical effects that

are at work may be much more subtle. We are currently in the process of analyzing whether bar-driven inflows, for example, might account for some of the trend internal to our COLD GASS sample.

In high redshift galaxies, however, the high values of sSFR are achieved simply because there is a *lot* of molecular gas. This leads us to speculate that at high redshifts the star formation bottleneck is no longer in the conversion of atomic to molecular gas. Indeed, the flat dependence of Ω_{HI} with redshift inferred from the abundance of damped Lyman alpha systems in high redshift quasar spectra would appear to rule out the presence of large HI reservoirs in high redshift galaxies (e.g. Hopkins et al. 2005). Although gas accretion rates are expected to be much larger at high redshifts, most of the gas must be transformed to molecular form almost immediately. The star formation bottleneck in high redshift galaxies may then have more to do with the formation of the proto-stars themselves.

ACKNOWLEDGMENTS

This work is based on observations carried out with the IRAM 30 m telescope. IRAM is supported by INSU/CNRS (France), MPG (Germany), and IGN (Spain). We sincerely thank the staff of the telescope for their help in conducting the COLD GASS observations.

RG and MPH are supported by NSF grant AST-0607007 and by a grant from the Brinson Foundation.

REFERENCES

- Abazajian K. N., Adelman-McCarthy J. K., Agüeros M. A., Allam S. S., Allende Prieto C., et al. 2009, *ApJS*, 182, 543
- Baan W. A., van Gorkom J. H., Schmelz J. T., Mirabel I. F., 1987, *ApJ*, 313, 102
- Bigiel F., Leroy A., Walter F., Brinks E., de Blok W. J. G., Madore B., Thornley M. D., 2008, *AJ*, 136, 2846
- Bolatto A. D., Leroy A. K., Rosolowsky E., Walter F., Blitz L., 2008, *ApJ*, 686, 948
- Boquien M., Bendo G., Calzetti D., Dale D., Engelbracht C., Kennicutt R., Lee J. C., van Zee L., Moustakas J., 2010, *ApJ*, 713, 626
- Bothwell M. S., Chapman S. C., Tacconi L., Smail I., Ivison R. J., Casey C. M., Bertoldi F., Beswick R., Biggs A., Blain A. W., Cox P., Genzel R., Greve T. R., Kennicutt R., Muxlow T., Neri R., Omont A., 2010, *MNRAS*, 405, 219
- Bouché N., Cresci G., Davies R., Eisenhauer F., Förster Schreiber N. M., Genzel R., Gillessen S., Lehnert M., et al. 2007, *ApJ*, 671, 303
- Brinchmann J., Charlot S., White S. D. M., Tremonti C., Kauffmann G., Heckman T., Brinkmann J., 2004, *MNRAS*, 351, 1151
- Bruzual G., Charlot S., 2003, *MNRAS*, 344, 1000
- Calzetti D., Kinney A. L., Storchi-Bergmann T., 1994, *ApJ*, 429, 582
- Catinella B., Haynes M. P., Giovanelli R., 2007, *AJ*, 134, 334
- Catinella B., Haynes M. P., Giovanelli R., Gardner J. P., Connolly A. J., 2008, *ApJ*, 685, L13
- Catinella B., Schiminovich D., Kauffmann G., Fabello S., Wang J., et al. 2010, *MNRAS*, 403, 683
- Chakrabarti S., Blitz L., 2009, *MNRAS*, 399, L118
- Chapman S. C., Blain A. W., Smail I., Ivison R. J., 2005, *ApJ*, 622, 772
- da Cunha E., Charmandaris V., Díaz-Santos T., Armus L., Marshall J. A., Elbaz D., 2010, *A&A*, 523, A78+
- Daddi E., Bournaud F., Walter F., Dannerbauer H., Carilli C. L., Dickinson M., Elbaz D., Morrison G. E., Riechers D., Onodera M., Salmi F., Krips M., Stern D., 2010, *ApJ*, 713, 686
- Downes D., Solomon P. M., 1998, *ApJ*, 507, 615
- Downes D., Solomon P. M., 2003, *ApJ*, 582, 37
- Engel H., Tacconi L. J., Davies R. I., Neri R., Smail I., Chapman S. C., Genzel R., Cox P., Greve T. R., Ivison R. J., Blain A., Bertoldi F., Omont A., 2010, *ApJ*, 724, 233
- Frazer D. T., Ivison R. J., Scoville N. Z., Yun M., Evans A. S., Smail I., Blain A. W., Kneib J., 1998, *ApJ*, 506, L7
- Fu J., Guo Q., Kauffmann G., Krumholz M. R., 2010, *MNRAS*, pp 1359+
- Gao Y., Solomon P. M., 2004, *ApJ*, 606, 271
- Genzel R., Baker A. J., Tacconi L. J., Lutz D., Cox P., Guilloteau S., Omont A., 2003, *ApJ*, 584, 633
- Genzel R., Tacconi L. J., Gracia-Carpio J., Sternberg A., Cooper M. C., et al. 2010, *MNRAS*, 407, 2091
- Giovanelli R., Haynes M. P., Kent B. R., Perillat P., Sain-tonge A., Brosch N., Catinella B., et al. 2005, *AJ*, 130, 2598
- Graciá-Carpio J., García-Burillo S., Planesas P., Fuente A., Usero A., 2008, *A&A*, 479, 703
- Graciá-Carpio J., Sturm E., Hailey-Dunsheath S., Fischer J., Contursi A., Poglitsch A., Genzel R., González-Alfonso E., et al. 2011, *ApJ*, 728, L7+
- Gratier P., Braine J., Rodriguez-Fernandez N. J., Schuster K. F., Kramer C., Xilouris E. M., Tabatabaei F. S., Henkel C., et al. 2010, *A&A*, 522, A3+
- Hainline L. J., Blain A. W., Smail I., Alexander D. M., Armus L., Chapman S. C., Ivison R. J., 2010, *ArXiv e-prints*
- Hopkins A. M., Rao S. M., Turnshek D. A., 2005, *ApJ*, 630, 108
- Howell J. H., Armus L., Mazzarella J. M., Evans A. S., Surace J. A., Sanders D. B., Petric A., Appleton P., et al. 2010, *ApJ*, 715, 572
- Johnson B. D., Schiminovich D., Seibert M., Treyer M., Martin D. C., Barlow T. A., Forster K., Friedman P. G., et al. 2007, *ApJS*, 173, 377
- Kennicutt Jr. R. C., 1989, *ApJ*, 344, 685
- Kennicutt Jr. R. C., 1998a, *ARA&A*, 36, 189
- Kennicutt Jr. R. C., 1998b, *ApJ*, 498, 541
- Kennicutt Jr. R. C., Calzetti D., Walter F., Helou G., Hollenbach D. J., Armus L., Bendo G., Dale D. A., et al. 2007, *ApJ*, 671, 333
- Kereš D., Katz N., Weinberg D. H., Davé R., 2005, *MNRAS*, 363, 2
- Kneib J., Neri R., Smail I., Blain A., Sheth K., van der Werf P., Knudsen K. K., 2005, *A&A*, 434, 819
- Krumholz M. R., Leroy A. K., McKee C. F., 2011, *ArXiv e-prints*
- Krumholz M. R., Matzner C. D., McKee C. F., 2006, *ApJ*, 653, 361

- Krumholz M. R., McKee C. F., Tumlinson J., 2009, *ApJ*, 699, 850
- Leroy A. K., Bolatto A., Gordon K., Sandstrom K., Gratier P., Rosolowsky E., Engelbracht C. W., Mizuno N., Corbelli E., Fukui Y., Kawamura A., 2011, *ArXiv e-prints*
- Leroy A. K., Walter F., Bigiel F., Usero A., Weiss A., et al. 2009, *AJ*, 137, 4670
- Leroy A. K., Walter F., Brinks E., Bigiel F., de Blok W. J. G., Madore B., Thornley M. D., 2008, *AJ*, 136, 2782
- Lotz J. M., Primack J., Madau P., 2004, *AJ*, 128, 163
- Magnelli B., Lutz D., Berta S., Altieri B., Andreani P., Aussel H., Castañeda H., Cava A., et al. 2010, *A&A*, 518, L28+
- Martig M., Bournaud F., Teyssier R., Dekel A., 2009, *ApJ*, 707, 250
- Martin D. C., Fanson J., Schiminovich D., Morrissey P., Friedman P. G., et al. 2005, *ApJ*, 619, L1
- McKee C. F., Ostriker E. C., 2007, *ARA&A*, 45, 565
- Meurer G. R., Heckman T. M., Calzetti D., 1999, *ApJ*, 521, 64
- Mo H. J., Mao S., White S. D. M., 1998, *MNRAS*, 295, 319
- Moran S. M., Kauffmann G., Heckman T. M., Gracia-Carpio J., Saintonge A., Catinella B., Wang J., Chen Y., et al. 2010, *ApJ*, 720, 1126
- Moshir M., Kopman G., Conrow T. A. O., 1992, *IRAS Faint Source Survey, Explanatory supplement version 2*
- Neri R., Genzel R., Ivison R. J., Bertoldi F., Blain A. W., Chapman S. C., Cox P., Greve T. R., Omont A., Frayer D. T., 2003, *ApJ*, 597, L113
- Noeske K. G., Weiner B. J., Faber S. M., Papovich C., Koo D. C., Somerville R. S., Bundy K., Conselice C. J., et al. 2007, *ApJ*, 660, L43
- Pérez-González P. G., Trujillo I., Barro G., Gallego J., Zamorano J., Conselice C. J., 2008, *ApJ*, 687, 50
- Pettini M., Pagel B. E. J., 2004, *MNRAS*, 348, L59
- Riechers D. A., Walter F., Carilli C. L., Bertoldi F., 2007, *ApJ*, 671, L13
- Rodighiero G., Cimatti A., Gruppioni C., Popesso P., Andreani P., et al. 2010, *A&A*, 518, L25+
- Rosolowsky E., Blitz L., 2005, *ApJ*, 623, 826
- Saintonge A., Kauffmann G., Kramer C., Tacconi L. J., Buchbender C., Catinella B., Fabello S., Gracia-Carpio J., et al. 2011, *ArXiv e-prints*
- Salim S., Rich R. M., Charlot S., Brinchmann J., Johnson B. D., et al. 2007, *ApJS*, 173, 267
- Sanders D. B., Mirabel I. F., 1985, *ApJ*, 298, L31
- Sanders D. B., Scoville N. Z., Soifer B. T., 1991, *ApJ*, 370, 158
- Schiminovich D., Catinella B., Kauffmann G., Fabello S., Wang J., et al. 2010, *MNRAS*, 408, 919
- Schinnerer E., Weiß A., Aalto S., Scoville N. Z., 2010, *ApJ*, 719, 1588
- Schmidt M., 1959, *ApJ*, 129, 243
- Schruba A., Leroy A. K., Walter F., Sandstrom K., Rosolowsky E., 2010, *ApJ*, 722, 1699
- Solomon P. M., Downes D., Radford S. J. E., Barrett J. W., 1997, *ApJ*, 478, 144
- Springob C. M., Haynes M. P., Giovanelli R., Kent B. R., 2005, *ApJS*, 160, 149
- Tacconi L. J., Genzel R., Neri R., Cox P., Cooper M. C., Shapiro K., Bolatto A., Bouché N., et al. 2010, *Nature*, 463, 781
- Tacconi L. J., Genzel R., Smail I., Neri R., Chapman S. C., et al. 2008, *ApJ*, 680, 246
- Tremonti C. A., Heckman T. M., Kauffmann G., Brinchmann J., Charlot S., White S. D. M., Seibert M., Peng E. W., Schlegel D. J., Uomoto A., Fukugita M., Brinkmann J., 2004, *ApJ*, 613, 898
- Verheijen M., van Gorkom J. H., Szomoru A., Dwarakanath K. S., Poggianti B. M., Schiminovich D., 2007, *ApJ*, 668, L9
- Walter F., Brinks E., de Blok W. J. G., Bigiel F., Kennicutt R. C., Thornley M. D., Leroy A., 2008, *AJ*, 136, 2563
- Wang J., Kauffmann G., Overzier R., Catinella B., Schiminovich D., Heckman T. M., Moran S. M., Haynes M. P., Giovanelli R., Kong X., 2010, *ArXiv e-prints*
- Wang J., Overzier R., Kauffmann G., von der Linden A., Kong X., 2010, *MNRAS*, 401, 433
- Wyder T. K., Martin D. C., Schiminovich D., Seibert M., Budavári T., et al. 2007, *ApJS*, 173, 293

APPENDIX A: STAR FORMATION RATES

We use a spectral energy distribution (SED) fitting technique to derive the star formation rate (SFR) for each galaxy in the COLD GASS sample. The Bruzual & Charlot (2003) population synthesis code is used to generate model galaxies with a range of ages, star formation histories, metallicities and dust attenuations and to create a library of model SEDs in 7 bands (FUV, NUV, u , g , r , i and z). For each galaxy, we evaluate the goodness-of-fit of each model SED and then estimate its SFR and dust attenuation factor as the χ^2 -weighted average of the model parameters.

This technique is very similar to Salim et al. (2007) in the way the metallicity, age and star formation history (SFH) priors are set. There are, however, two main differences compared to their methodology: (1) we only use an exponentially declining SFH without bursts, because massive galaxies such as those in the COLD GASS sample do not tend to have bursty SFHs, and (2) we use an extinction coefficient (A_V) that depends on NUV- r colour, after calibration using a reference sample with direct measurement of the SFR through UV and infrared measurements. The technique and the calibration of A_V are explained in more detail below.

As pointed out by Salim et al. (2007) and Wang et al. (2010), the derived dust attenuation (and thus SFR) is sensitive to the assumed prior distribution of A_V . A direct estimate of A_V in a galaxy is possible only if we know its UV through far-IR SED. This is not the case for our sample, so we have assumed a different prior A_V distribution for each individual galaxy, constrained by an indirect estimate of A_V in the galaxy. Two different methods of estimating the A_V prior are considered: the measured Balmer decrement from the SDSS spectrum, and a combination of D4000 and NUV- r colour (Johnson et al. 2007). The former method measures the extinction experienced by stars located in HII regions (Calzetti et al. 1994) in the central 3'' of the galaxy, while the latter is a rough estimate of the attenuation of the light from stars with ages of a few hundred million years (see also Schiminovich et al. 2010). We denote the A_V measured from these two methods as $A_V(B)$ and $A_V(N)$, respectively.

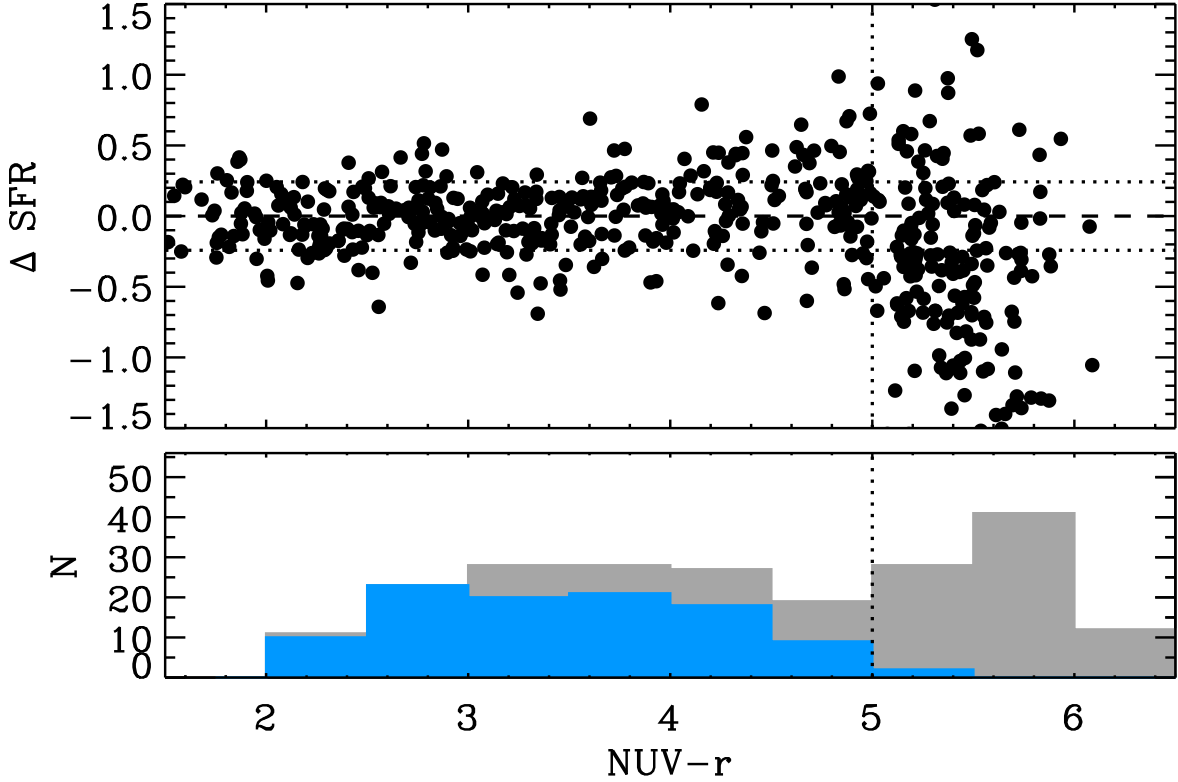


Figure A1. Difference in the SFRs measured using the SED-fitting technique and a combination of UV and IR photometry ($\Delta\text{SFR} = \log(\text{SFR}_{\text{SED}}) - \log(\text{SFR}_{\text{tot}})$). The values of ΔSFR are plotted as a function of $\text{NUV}-r$ colour (top panel), and the colour distribution of the COLD GASS sample is shown in the bottom panel (in gray the complete sample, in blue the galaxies with CO detection). Over the colour range where CO detections are possible ($\text{NUV}-r < 5$), the scatter between the two SFR measurements is only 0.24 dex, with no systematic offset.

We make use of the GMACS (Galaxy Multiwavelength Atlas From Combined Surveys) sample (Johnson et al. 2007) to tune our choice of the assumed prior distribution of A_V in the model library, and to test the robustness of the SFR derived from the SED fitting. The $70\mu\text{m}$ fluxes are converted into total infrared luminosities (L_{TIR}), taking into account a correction factor from the ratio of the observed fluxes at $24\mu\text{m}$ and $8\mu\text{m}$ (Boquien et al. 2010). We apply the dust model from Meurer et al. (1999) and the extinction curve from Calzetti et al. (1994) and calculate A_V from the ratio of L_{TIR} over the luminosity in the FUV ($A_V(\text{IRX})$). We use the Kennicutt (1998a) relation to convert L_{TIR} to SFR (SFR_{TIR}) and divide it by a factor of 1.7 to account for the difference between Salpeter IMF and Chabrier IMF. We calculate SFR from obscured FUV luminosity (SFR_{FUV}) using the formula from Salim et al. (2007). The total star formation rate for the GMACS galaxies is therefore obtained as $\text{SFR}_{\text{tot}} = \text{SFR}_{\text{TIR}} + \text{SFR}_{\text{UV}}$, with the latter not corrected for dust extinction.

Different prescriptions for A_V based on the SDSS data are tested against the directly measured values of $A_V(\text{IRX})$. We find that different techniques to measure for A_V minimize best the scatter with $A_V(\text{IRX})$ in different $\text{NUV}-r$ colour intervals, and therefore adopt the following prescription:

$$A_V(\text{best}) = \begin{cases} A_V(B) - 0.052(\text{NUV} - r) & \text{if } \text{NUV} - r < 2.5 \\ 0.5(A_V(B) + A_V(N)) & \text{if } 2.5 < \text{NUV} - r < 3.5 \\ A_V(N) & \text{if } 3.5 < \text{NUV} - r < 5.0 \\ 1.5 & \text{if } \text{NUV} - r > 5. \end{cases} \quad (\text{A1})$$

Therefore, when we estimate the SFR for an individual galaxy, we adopt a Gaussian prior distribution of A_V based on its observed colour that peaks at $A_V(\text{best})$ as given in Equation A1 and has a width of $\sigma = 0.15$. We compare SFR from the SED fitting method with the “true” SFR_{tot} measured from the UV and IR photometry in Figure A1. The two sets of SFRs are very consistent when $\text{NUV}-r < 5$, with a scatter of 0.24 dex in their log difference. The scatter over the full colour distribution is 0.37 dex, because of the low S/N in the GALEX images for the redder galaxies. This, however, has no influence on the results of this paper, since all COLD GASS galaxies detected in CO have $\text{NUV}-r < 5$ where the SED-fitting technique produces reliable SFR measurements.

Another approach to measure SFRs for the COLD GASS galaxies would have been to correct the GALEX FUV flux using $A_V(\text{best})$ to infer the total SFR ($\text{SFR}_{\text{FUV,cor}}$), instead of relying on SED fitting using a model library. This was the approach taken in Johnson et al. (2007), and we test it on the GMACS sample. The scatter in the log difference of SFR_{tot} and $\text{SFR}_{\text{FUV,cor}}$ is 0.29 dex for galaxies with $\text{NUV}-r < 5$. Over the same colour range, the scatter

between SFR_{tot} and SFR_{SED} is 0.24, indicating that information is gained by using the full 7 optical and UV bands from SDSS and GALEX in the determination of the SFRs, if the dust attenuation prior distribution can be well constrained.

APPENDIX B: RESIDUALS OF THE MOLECULAR GAS DEPLETION TIME RELATIONS

As explained in Section 3.1 and shown in Figure 3, the molecular gas depletion time ($t_{dep}(\text{H}_2)$) correlates best with specific star formation rate (sSFR). To investigate what other physical parameters may be at play in setting this relation, we examine here the residuals of the sSFR- $t_{dep}(\text{H}_2)$ relation as a function of the other global parameters considered in this study. The (data - fit prediction) residuals are shown in Figure B1, where a positive residual therefore indicates a longer depletion time than average at fixed sSFR.

The only two parameters upon which the residuals depend are the measures of smoothness and asymmetry (Figure B1 h and i). However, the trends are driven mostly by a small number of points at both low and high values of Smth and Asym, and the amplitude of the trend seen in the binned values is smaller than the overall calibration accuracy of the star formation rates (Appendix A) and the uncertainty on the molecular gas masses. Furthermore, if we were instead to show the residuals of the stellar mass- $t_{dep}(\text{H}_2)$ relation, the trend seen with Smth and Asym is even weaker. We therefore conclude that there is no significant third parameter dependence among the quantities we have examined. We will examine this issue in more detail in a later paper.

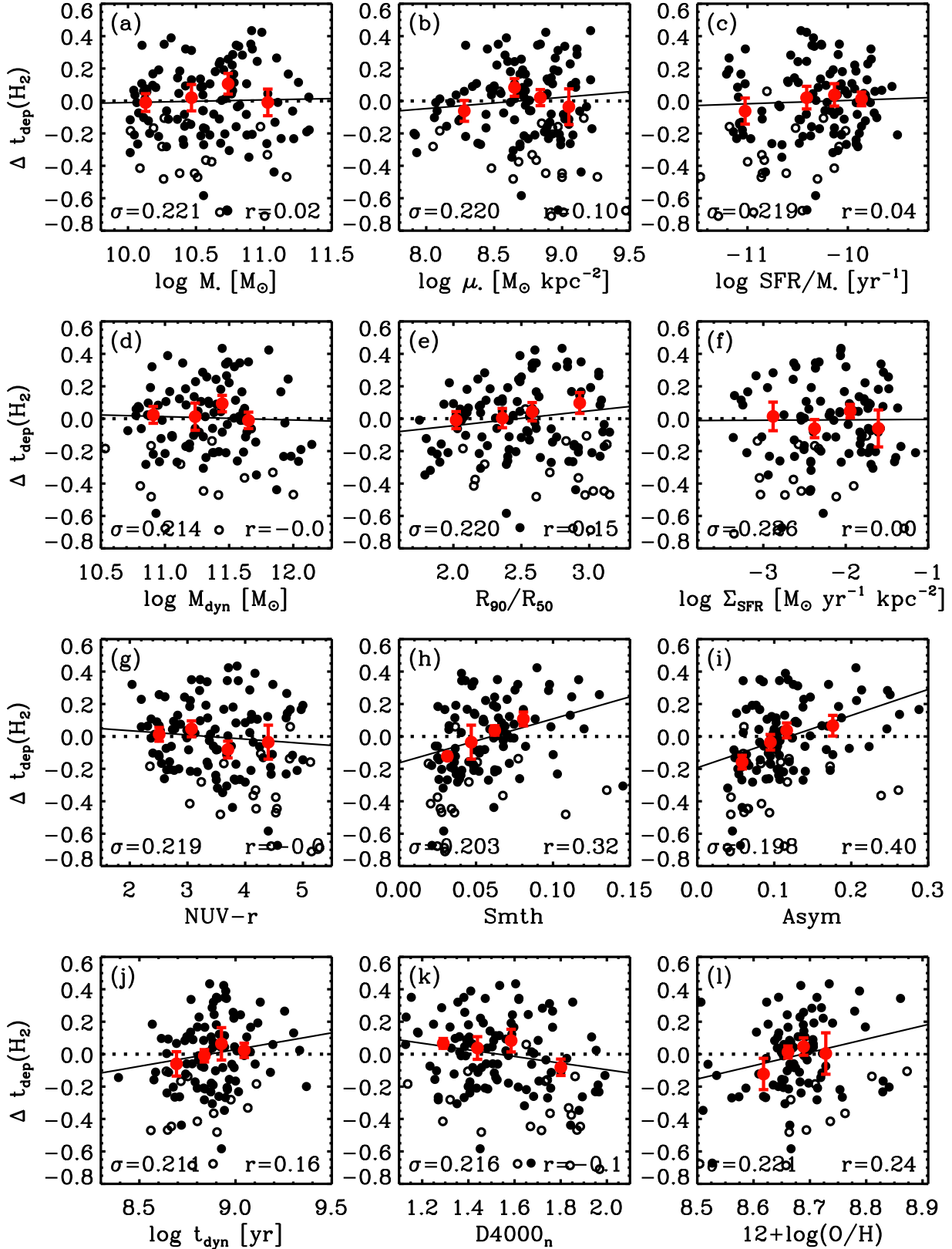


Figure B1. Residuals of the sSFR- $t_{\text{dep}}(\text{H}_2)$ relation of Figure 3c, as a function of 12 different global measurements for the COLD GASS galaxies with secure (filled circles) and tentative (open circles) CO detections. The red symbols show the mean value of the residuals in equally-populated bins of the x -axis parameter. The correlation coefficient (r) of the data in each plane as well as the scatter around the best fit relation (σ) are given in each case.